

NATIONAL UNIVERSITY OF HO CHI MINH CITY  
UNIVERSITY OF SCIENCE  
FACULTY OF PHYSICS- ENGINEERING PHYSICS

Vo Chau Duc Phuong

CALCULATION OF THE LINEAR-ABSORPTION SPECTRUM OF  
AN IDEAL TWO-DIMENSIONAL SYSTEM OF  $\text{MoS}_2$

Graduation Bachelor Thesis  
Merits Program

Ho Chi Minh city, July-2024

NATIONAL UNIVERSITY OF HO CHI MINH CITY  
UNIVERSITY OF SCIENCE  
FACULTY OF PHYSICS- ENGINEERING PHYSICS

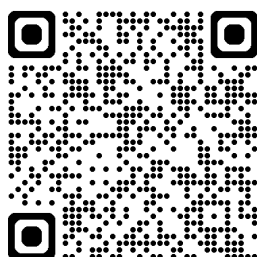
Vo Chau Duc Phuong

Calculation of the Linear-Absorption Spectrum of  
an Ideal Two-Dimensional System of  $\text{MoS}_2$

Graduation Bachelor Thesis  
Merits Program

Supervisor: Dr. Huynh Thanh Duc

E-pdf version:



Ho Chi Minh city, July-2024

## **Commitment**

I commit to independently conducting the calculation of the linear-absorption spectrum of an ideal two-dimensional system of  $\text{MoS}_2$  for my bachelor thesis, under the supervision of Dr. Huynh Thanh Duc, and with guidance from Master Le Minh Chau.

**STUDENT**

# Acknowledgments

Even though I still have much more to study to achieve my dream of becoming a physicist, this work marks the first step on my path. I couldn't have completed this work without the guidance of Dr. Huynh Thanh Duc and Master Le Minh Chau at the Institute of Physics, Ho Chi Minh City. I am truly grateful to them.

I also want to express my gratitude to Dr. Vu Quang Tuyen, Dr. Vo Quoc Phong, and Dr. Nguyen Huu Nha, three lecturers in the Department of Theoretical Physics. They have guided me throughout my time at the department and at the University of Science, Ho Chi Minh City.

Other thanks go to Pham Nhat Minh, Le Huu Thong, Le Thi Lien, Kien Le, and Phan Anh Luan (Luancio)... I had multiple interesting discussions for a better understanding of my and their research interest.

# Contents

<b>1</b>	<b>Introduction</b>	<b>7</b>
<b>2</b>	<b>Theories</b>	<b>10</b>
2.1	Tight-Binding Theories . . . . .	10
2.2	Three Band Tight-Binding Model . . . . .	11
2.3	System Hamiltonian . . . . .	14
2.3.1	First Quantization Hamiltonian . . . . .	14
2.3.2	Second Quantization Hamiltonian . . . . .	15
2.4	Semiconductor Bloch Equation . . . . .	17
2.5	Polarization Density . . . . .	18
<b>3</b>	<b>Numerical Methods</b>	<b>19</b>
3.1	Numerical Sum Over k-Space . . . . .	19
3.2	Cut-off K-point Technique . . . . .	20
3.3	Absorption and Electromagnetic Field . . . . .	21
<b>4</b>	<b>Results and Discussion</b>	<b>22</b>
<b>5</b>	<b>Conclusion and Further Research</b>	<b>26</b>
	<b>Appendices</b>	<b>27</b>
<b>A</b>	<b>Coulomb matrix elements</b>	<b>27</b>
<b>B</b>	<b>Equation of Motion</b>	<b>29</b>
<b>C</b>	<b>Dipole Matrix Elements</b>	<b>31</b>

## List of Figures

1	TMD structure and its first Brillouin zone . . . . .	11
2	Band structure of MoS <sub>2</sub> material along $M \rightarrow -K \rightarrow \Gamma \rightarrow K \rightarrow M$ direction . .	13
3	Rhombus primitive unit cell in compare with hexagon primitive unit cell (the first Brillouin zone) . . . . .	19
4	New basis Based on the rhombus unit vectors . . . . .	20
5	k-radius show the cutoff circle around K' points . . . . .	21
6	Electric field on Ox direction and its Fourier Transform . . . . .	22
7	absorption spectrum of MoS <sub>2</sub> . . . . .	23
8	Absorption Spectrum with difference $T_2$ . . . . .	24
9	Absorption Spectrum with difference dielectric $\varepsilon$ and without Coulomb interaction . . . . .	25
10	Absorption Spectrum with difference number of k-points . . . . .	25

## List of Tables

1	Fitting parameters in three-band tight-binding model for $MoS_2$ . . . . .	13
2	Exciton binding energy with difference dielectric . . . . .	23

# Thesis Information

Name of Thesis: Calculation of the Linear-Absorption Spectrum of MoS<sub>2</sub>

Major: Physics

Specialty: Theoretical Physics

Name of Student: Vo Chau Duc Phuong

Student ID: 20130008

Academic Year: 2020

Supervisor: Dr. Huynh Thanh Duc

## Abstract

Transition metal dichalcogenides (TMD) are promising semiconductors due to their extraordinary electronic and optoelectronic properties. Before calculating the nonlinear optical properties of this material, we need to calculate the linear absorption spectrum. In monolayer TMD, the Coulomb interaction heavily influences the increase in exciton binding energies. Therefore, the independent electron approximation model is unreliable for simulating the experiment, especially in low-dimensional systems. In this work, we use a minimum three-band tight-binding Hamiltonian for the band structure calculation and the semiconductor Bloch equations to model the response of electron density in material to a laser over time to calculate the linear absorption spectra (LAS) and extract the exciton binding energy from it.

## Novelty Of Thesis

Our calculation on exciton binding energy (0.25 eV) based on this model proves to agree with the experiment. It proves to be more accurate than some previous theories, which predicted exciton binding energy too large (0.5-1 eV).

## Applications/ Applicability/ Perspective

From this work, we can use it to calculate other linear- and nonlinear-effects that are affected by exciton binding energy such as photo-current, high harmonic generation, and high-order sideband generation. For further work, we can increase the density of the k-point for better convergence results. Take into account the shield coulomb interaction when increasing the density of electrons on the conduction bands when excess of the low excitation limit for full absorption spectra.

**SUPERVISOR**

**STUDENT**

**CERTIFICATION  
UNIVERSITY OF SCIENCE  
PRESIDENT**



# 1 Introduction

When exploring the properties of a material, the linear absorption spectrum is a crucial tool. This spectrum provides valuable insights into the material’s electronic structure by precisely measuring the energy of absorbed photons. This analysis helps us understand the material’s energy levels, transitions between states, and the nature of electron excitation. By examining the absorption peaks and bands, we can calculate important coefficients such as absorbance and extinction coefficients, which are vital in various scientific and industrial applications.

The photovoltaic effect is the generation of a photo-current and voltage in a material under illumination, caused by charge separation involving two or more material components<sup>1</sup>. In conventional solar cells that use a p-n junction for photo-electric conversion, the maximum efficiency is limited to about 33% when the band gap of the material is 1.4 eV<sup>2</sup>. However, the bulk photovoltaic (BPV) effect, which is a second-order non-linear optical phenomenon occurring when non-centrosymmetric materials are illuminated by a laser, is expected to surpass the Shockley-Queisser limit. Under linearly polarized laser illumination, electrons transition from valence bands to conduction bands, creating a shift current by changing the electron’s center of symmetry. When circularly polarized lasers are used, only electrons with a specific spin orientation, dependent on the laser’s circular direction, are stimulated, creating an injection current. When accounting for electron-electron Coulomb interactions, the asymmetry of the Coulomb interaction results in an asymmetry of the electron density distribution, which creates a ballistic current. The complexity of including the electron-electron Coulomb interaction sometimes causes it sometimes be ignored, but this contribution is not small<sup>3</sup>.

The researcher has dedicated many years to studying Graphene, with hopes that it could potentially serve as the new silicon, enabling the continuation of Moore’s law on the CPU chip dice. However, in recent years, the number of papers on Graphene properties has reached thousands yearly, indicating that research on ‘simple graphene’ has peaked.<sup>4</sup> Therefore, the researchers shifted their focus from working solely with Graphene to exploring applications and other two-dimensional materials. Atomically thin two-dimensional (2D) forms of layered transition metal dichalcogenides (TMD) have recently gained significant scientific and technological interest since the first five years of the Graphene boom<sup>4;5</sup>.

TMD has the chemical composition  $MX_2$ , so it has a wide range of materials. They include both metals and semiconductors, for example NbS<sub>2</sub>, NbSe<sub>2</sub>, TaS<sub>2</sub>, TaSe<sub>2</sub>,  $\beta$ -MoT<sub>2</sub> and Td-WTe<sub>2</sub> are bulk metals while the ReS<sub>2</sub>, ZrS<sub>2</sub>, MoS<sub>2</sub>, WS<sub>2</sub>, MoSe<sub>2</sub>, WSe<sub>2</sub> and  $\alpha$ -MoTe<sub>2</sub> are semiconductors. The structure of TMD consists of multiple monolayers bonded by van der Waals forces, with in-plane stability ensured by strong covalent bonds.

TMD exhibits non-centrosymmetry in monolayers form, resulting in unique properties in electronic, spintronics, optoelectronics, superconduction, and valleytronic applications<sup>6;7</sup>. Among various transition metal dichalcogenides, the group-VIB (M = Mo, W; X = S, Se) is

stable in both mono- and few-layers in the air at room temperature<sup>4</sup>. Additionally, significant spin-orbit coupling in TMD creates a considerable split in the band structure valley. These two-dimensional semiconductors have a direct band gap in the visible frequency range, stable and excellent mobility at room temperature<sup>1;5</sup>, and promise to become a good candidate for electronic and optoelectronic applications. Its nanotube structure has been researched and also shows its potential to become the new solar cell material<sup>1;8-10</sup>.

The low dimension system causes the reduced screening of Coulomb interaction outside the monolayer's plane, resulting in larger exciton binding energies<sup>11;12</sup>. These binding energies are notably higher than those observed in typical III-V materials, implying that many-body interactions play a key role in determining the electronic and optical properties of these materials. In some previous work, only the nearly free electron approximation has been taken into account and did not give good accuracy on the results as the key role of many-body interactions in the system in simulating the photoelectric currents. Furthermore, previous theoretical works have predicted the binding energy too large<sup>13-16</sup> when compared with experiment<sup>12</sup> and other more accurate theoretical works<sup>11;12</sup>. Therefore, this thesis will focus on calculating the exciton binding energy through the absorption spectrum to fit the results with experiments and other theoretical work.

In our current research, our main objective is to identify the appropriate model for estimating the exciton binding energy while aligning with experimental data. The key challenge is to identify a model that balances simplicity and accuracy. Our primary focus is on investigating the properties of TMD. Several models, such as ab initio calculations<sup>11;13-16</sup> and parabola approximation<sup>17;18</sup>, have been developed and employed to simulate the band structure. It is important to note that these models have limitations as they can only be calculated around highly symmetric points and not across the entire Brillouin zone (BZ). In our study, we are using a three-band tight-binding model to calculate properties across the entire BZ, which should give us results that better match experimental data.

In this work, we use the minimal three-band tight-binding Hamiltonian<sup>19</sup> to calculate the band structure by determining the eigenvalues at each k-point. The momentum matrix for the velocity gauge matrix will be calculated using finite differentiation and then utilized to compute the dipole matrix. We plan to solve the Semiconductor Bloch Equations (SBE) using the Runge-Kutta 4th-order method to numerically find the time-dependent density evolution. Based on this density, we can derive the polarization, current density, and other measurable physical observations. After obtaining the polarization density, we will perform a Fourier transform to obtain the absorption spectrum.

In our analysis, we concentrate on the low excitation regime to examine the linear absorption spectra. We were able to concentrate on scenarios where the electron density in the conduction bands is significantly lower than that in the valence bands. The results show a significant exciton binding energy, which closely matched both experimental measurements

and theoretical expectations. These discoveries allow us to predict the existence of smaller excitons and use the binding energy to investigate other effects influenced by the Coulomb interaction.

The main content of this thesis will be included:

- Briefing the tight-binding theory with some important approximations such as independent electron approximation and tightly bound electron approximation. Then the electron wave functions will be constructed based on the linear combination of atomic orbitals. Introducing the parameters of this model: hopping energies and overlap density. In our concern with MoS<sub>2</sub>, the parameters of the tight-binding model will be obtained from the three-band tight-binding model presented in Ref. <sup>19</sup>. This model is chosen to fit with the band structure obtained from ab initio calculation in the entire first Brillouin zone. Deriving the Hamiltonian for a multi-body electron system in interaction with an external electromagnetic field in velocity gauge, the semiconductor Bloch equations describe the dynamic optoelectronic response that includes the electron-electron Coulomb interaction in the Hatree-Fock approximation.
- Introducing the formulas to calculate the dipole matrix and microscopic polarization density, the rhombus basis, and the basis transformation between rectangular and rhombus basis. Presenting the cut-off technique to reduce workloads in many-body interaction calculation when increasing the number of k-points in a discrete k-grid. Introducing parameters for the linear absorption spectrum formula, parameters for the external field, and its Fourier transform.
- Results and discussion on the aligning between numerical results and measurement. Conclusion on the exciton binding energy and discussion on the relation between dielectric, relaxation, and density of k-point in k-grid and the absorption spectrum. Further discussion on the disadvantages encountered in the calculation process and suggesting the overcome path.

## 2 Theories

### 2.1 Tight-Binding Theories

The Hamiltonian of a multi-body system, when Coulomb interaction between electrons is not taken into account, is the sum of independent electron Hamiltonians:

$$H = \sum_i H_{1e}(\mathbf{r}_i). \quad (1)$$

In which,  $H_{1e}(\mathbf{r}_a)$  is the single electron Hamiltonian. In the independent electron approximation, the stationary state of an electron in a solid is presented by the one-particle time-independent Schrödinger equation:

$$H_{1e}\psi_{\lambda\mathbf{k}}(\mathbf{r}) = \left( -\frac{\hbar^2\nabla^2}{2m} + V_0(\mathbf{r}) \right) \psi_{\lambda\mathbf{k}}(\mathbf{r}) = \varepsilon_{\lambda}(\mathbf{k})\psi_{\lambda\mathbf{k}}(\mathbf{r}). \quad (2)$$

Where  $V_0$  is the periodic potential of ions,  $V_0(\mathbf{r}) = V_0(\mathbf{r} + \mathbf{R}_n)$ , in which  $\mathbf{R}_n$  is a lattice vector.  $\psi_{\lambda\mathbf{k}}(\mathbf{r})$  and  $\varepsilon_{\lambda}(\mathbf{k})$  are respectively the wave function and energy of electron band  $\lambda$  and wave vector  $\mathbf{k}$ . The electrons are tightly bound to the atom to which they belong and have limited interaction with surrounding atoms. Therefore, the wave function of an electron will have the similar form of well known atomic orbital and we can describe it in the form of linear combination of atomic orbitals (LCAO):

$$\psi(\mathbf{r}) = \sum_{n=1}^N \sum_{c=1}^{N_c} \sum_{\alpha=1}^{N_{orb}} c_{\alpha c}(\mathbf{R}_n) \phi_{\alpha}(\mathbf{r} - \mathbf{R}_n - \mathbf{r}_c). \quad (3)$$

Here,  $\phi_{\alpha}$  is orbital wave function of an atomic,  $\mathbf{R}_n$  is position of Bravais unit cell,  $\mathbf{r}_c$  is relative position of the atoms in that cell,  $N_{orb}$  is number of orbital of an atom,  $N_c$  is number of atom in an unit cell, and  $N$  is the number of unit cells in the lattice. Based on LCAO wave function, we can construct the Bloch wave function in the following form:

$$\psi_{\mathbf{k}}(\mathbf{r}) = \sum_{c=1}^{N_c} \sum_{\alpha=1}^{N_{orb}} C_{\alpha c}(\mathbf{k}) \sum_{n=1}^N e^{i\mathbf{k}(\mathbf{R}_n + \mathbf{r}_c)} \phi_{\alpha}(\mathbf{r} - \mathbf{R}_n - \mathbf{r}_c) \quad (4)$$

This wave function satisfies the Bloch theorem. Substituting Eq. (4) into Eq. (2) then multiplying with  $e^{i\mathbf{k}\mathbf{r}_{c'}} \phi_{\alpha'}^*(\mathbf{r} - \mathbf{r}_{c'})$  on the left, and taking the integral over  $\mathbf{r}$ , we obtain:

$$\sum_{c=1}^{N_c} \sum_{\alpha=1}^{N_{orb}} (H_{\alpha'c',\alpha c}(\mathbf{k}) - \varepsilon(\mathbf{k})S_{\alpha'c',\alpha c}(\mathbf{k})) C_{\alpha c}(\mathbf{k}) = 0. \quad (5)$$

Where

$$H_{\alpha'c',\alpha c}(\mathbf{k}) = \sum_{n=1}^N e^{i\mathbf{k}(\mathbf{R}_n + \mathbf{r}_c - \mathbf{r}_{c'})} \int d\mathbf{r} \phi_{\alpha'}^*(\mathbf{r} - \mathbf{r}_{c'}) H_{1e} \phi_{\alpha}(\mathbf{r} - \mathbf{R}_n - \mathbf{r}_c), \quad (6)$$

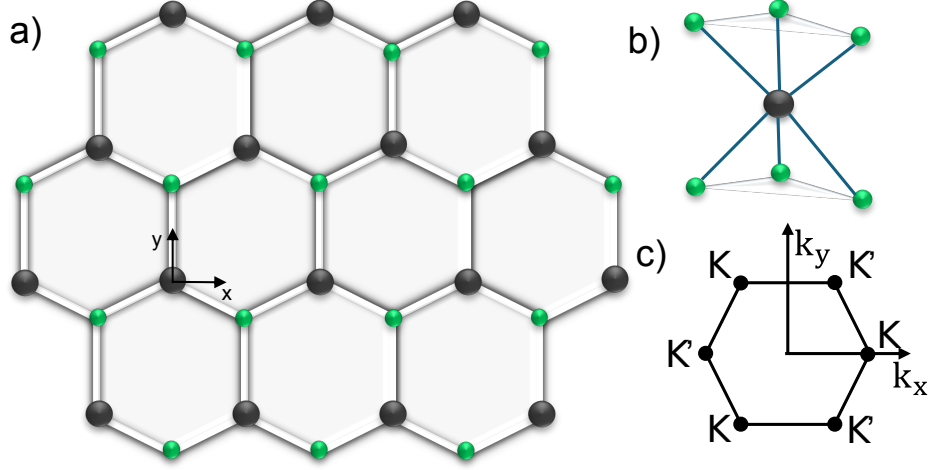


Figure 1: (a) Top view of monolayer  $MX_2$ . The large sphere is  $M$  atom and the small sphere is  $X$  atom. (b) sideview of monolayer  $MX_2$ . (c) The first Brillouin zone and high symmetry points in two dimensional  $k$ -space.

$$S_{\alpha'c',\alpha c}(\mathbf{k}) = \sum_{n=1}^N e^{i\mathbf{k}(\mathbf{R}_n + \mathbf{r}_c - \mathbf{r}_{c'})} \int d\mathbf{r} \phi_{\alpha'}^*(\mathbf{r} - \mathbf{r}_{c'}) \phi_{\alpha}(\mathbf{r} - \mathbf{R}_n - \mathbf{r}_c) \quad (7)$$

are the Hamiltonian matrix and overlap integral, respectively. By solving Eq. (5) at several  $k$ -points, we will have the wave functions and band structure  $\varepsilon_{\lambda}(\mathbf{k})$ . In the tight-binding theory, these integrals are given as semi-empirical parameters.

## 2.2 Three Band Tight-Binding Model

In previous ab initio calculations<sup>20–24</sup>, Xiao et al. discovered that the monolayer of  $MX_2$  with  $D_{3h}$  point-group symmetry has a structure as shown in Fig. 1. They found that the Bloch states of the monolayer  $MoS_2$  near the band edges are primarily composed of  $Mo-d$  orbitals, particularly the  $d_{z^2}$ ,  $d_{xy}$ , and  $d_{x^2-y^2}$  orbitals. To accurately capture the band-edge properties in the  $K$  and  $K'$  valleys, they developed an approximate model for group VII-B TMD consisting of only these three bands and neglecting  $X-p$  orbitals, and then extended it to fit the entire Brillouin Zone<sup>19</sup>. Denote three  $M$ - $d$  bands as:

$$|\phi_1\rangle = d_{z^2}, \quad |\phi_2\rangle = d_{xy}, \quad |\phi_3\rangle = d_{x^2-y^2}. \quad (8)$$

As discussed above, the Bloch states near the band edges mostly consist of  $Mo$ - $d$  orbital, therefore we ignore the  $\mathbf{r}_c$  and the sum over it in hopping energy (6). Each pair of difference basis is assumed to be orthogonal; therefore the overlapping matrix element become:

$$S_{\alpha,\alpha'}(\mathbf{k}) = \delta_{\alpha\alpha'}.$$

The hopping energies eq.(6) between the atomic orbitals  $|\phi_\mu\rangle$  at 0 and  $|\phi_{\mu'}\rangle$  at lattice vector  $\mathbf{R}$  can be obtained as:

$$H_{\mu\mu'}(\mathbf{k}) = \sum_{\mathbf{R}} e^{i\mathbf{k}\cdot\mathbf{R}} \langle \phi_\mu(\mathbf{r}) | \hat{H} | \phi_{\mu'}(\mathbf{r} - \mathbf{R}) \rangle.$$

Confined by the symmetry of the system, Tight-binding Hamiltonian have the form:

$$H^{TNN}(\mathbf{k}) = \begin{pmatrix} V_0 & V_1 & V_2 \\ V_1^* & V_{11} & V_{12} \\ V_2^* & V_{12}^* & V_{22} \end{pmatrix}, \quad (9)$$

where

$$\begin{aligned} V_0 &= \varepsilon_1 + 2t_0(2\cos\alpha\cos\beta + \cos 2\alpha) + 2r_0(2\cos 3\alpha\cos\beta + \cos 2\beta), \\ \text{Re}[V_1] &= -2\sqrt{3}t_2\sin\alpha\sin\beta + 2(r_1 + r_2)\sin 3\alpha\sin\beta - 2\sqrt{3}u_2\sin 2\alpha\sin 2\beta, \\ \text{Im}[V_1] &= 2t_1\sin\alpha(2\cos\alpha + \cos\beta) + 2(r_1 - r_2)\sin 3\alpha\cos\beta + 2u_1\sin 2\alpha(2\cos 2\alpha + \cos 2\beta) \\ \text{Re}[V_2] &= 2t_2(\cos 2\alpha - \cos\alpha\cos\beta) - \frac{2}{\sqrt{3}}(r_1 + r_2)(\cos 3\alpha\cos\beta - \cos 2\beta) + 2u_2(\cos 4\alpha - \cos 2\alpha\cos 2\beta), \\ \text{Im}[V_2] &= 2\sqrt{3}t_1\cos\alpha\sin\beta + \frac{2}{\sqrt{3}}\sin\beta(r_1 - r_2)(\cos 3\alpha + 2\cos\beta), \\ V_{11} &= \varepsilon_2 + (t_{11} + 3t_{22})\cos\alpha\cos\beta + 2t_{11}\cos 2\alpha + 4r_{11}\cos 3\alpha\cos\beta \\ &\quad + 2(r_{11} + \sqrt{3}r_{12})\cos 2\beta + (u_{11} + 3u_{22})\cos 2\alpha\cos 2\beta + 2u_{11}\cos 4\alpha, \\ \text{Re}(V_{12}) &= \sqrt{3}(t_{22} - t_{11})\sin\alpha\sin\beta + 4r_{12}\sin 3\alpha\sin\beta + \sqrt{3}(u_{22} - u_{11})\sin 2\alpha\sin 2\beta, \\ \text{Im}[V_{12}] &= 4t_{12}\sin\alpha(\cos\alpha - \cos\beta) + 4u_{12}\sin 2\alpha(\cos 2\alpha - \cos 2\beta), \\ V_{22} &= \varepsilon_2 + (3t_{11} + t_{22})\cos\alpha\cos\beta + 2t_{22}\cos 2\alpha + 2r_{11}(2\cos 3\alpha\cos\beta + \cos 2\beta) \\ &\quad + \frac{2}{\sqrt{3}}r_{12}(4\cos 3\alpha\cos\beta - \cos 2\beta) + (3u_{11} + u_{22})\cos 2\alpha\cos 2\beta + 2u_{22}\cos 4\alpha, \end{aligned}$$

and

$$(\alpha, \beta) = \left(\frac{1}{2}k_x a, \frac{\sqrt{3}}{2}k_y a\right), \quad (10)$$

11 additional parameters shown in table 1 obtained by fitting with FP calculation results. Due to the heavy transition-metal atom M, its spin orbit coupling (SOC) can be large. For simplicity, only the on-site contribution, namely, the  $\mathbf{L}\cdot\mathbf{S}$  term from M atoms, is considered. Using the basis  $\{|d_{z^2}, \uparrow\rangle, |d_{xy}, \uparrow\rangle, |d_{x^2-y^2}, \uparrow\rangle, |d_{z^2}, \downarrow\rangle, |d_{xy}, \downarrow\rangle, |d_{x^2-y^2}, \downarrow\rangle\}$ , the contribution of SOC to the Hamiltonian can be written as

$$H' = \lambda \mathbf{L}\cdot\mathbf{S} = \frac{\lambda}{2} \begin{pmatrix} L_z & 0 \\ 0 & -L_z \end{pmatrix}. \quad (11)$$

In which,

$$L_z = \begin{pmatrix} 0 & 0 & 0 \\ 0 & 0 & 2i \\ 0 & -2i & 0 \end{pmatrix}, \quad (12)$$

$\varepsilon_1$	$\varepsilon_2$	$t_0$	$t_1$	$t_2$	$t_{11}$	$t_{12}$	$t_{22}$	$r_0$	$r_1$
$r_2$	$r_{11}$	$r_{12}$	$u_0$	$u_1$	$u_2$	$u_{11}$	$u_{12}$	$u_{22}$	$\lambda$
0.820	1.931	-0.176	-0.101	0.531	0.084	0.169	0.070	0.070	-0.252
0.084	0.019	0.093	-0.043	0.047	0.005	0.304	-0.192	-0.162	0.073

Table 1: Fitting parameters in three-band tight-binding model for local-density approximation (LDA) cases for  $MoS_2$ .<sup>19</sup>

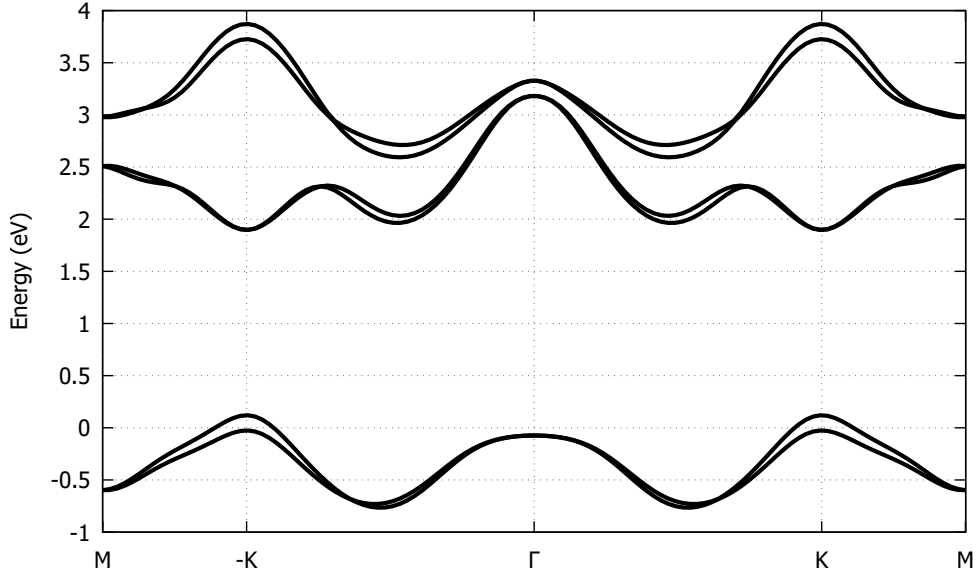


Figure 2: Band structure of monolayer-MoS<sub>2</sub> along  $M \rightarrow -K \rightarrow \Gamma \rightarrow K \rightarrow M$  direction, SOC causes huge splits in band-structure at K and  $-K$  points.

is the matrix of  $\hat{L}_z$  (z component of the orbital angular momentum) in basis of  $d_{z^2}$ ,  $d_{xy}$  and  $d_{x^2-y^2}$ , and  $\lambda$  is characterized for the strength of the SOC. Under these basis, the matrix elements of  $\hat{L}_x$  and  $\hat{L}_y$  are all zeros. Therefore the Hamiltonian with SOC have the form:

$$H(\mathbf{k}) = H_{SOC}(\mathbf{k}) = I_2 \otimes H^{TNN}(\mathbf{k}) + H' = \begin{bmatrix} H(\mathbf{k}) + \frac{\lambda}{2}L_z & 0 \\ 0 & H_0(\mathbf{k}) - \frac{\lambda}{2}L_z \end{bmatrix}. \quad (13)$$

By finding eigenvalue of Hamiltonian  $H$  in each  $\mathbf{k}$  point on entire BZ, the bands structure will be obtained. The bands structure with the huge bands split at the K and K' point of MoS<sub>2</sub> is caused by SOC is shown in fig.2.

## 2.3 System Hamiltonian

### 2.3.1 First Quantization Hamiltonian

For the accounting the Coulomb interaction between electron-electron in the many-body system, the system Hamiltonian can be written in form:

$$H = H^0 + H^{Coul} = \sum_i H_{1e}(\mathbf{r}_i) + \frac{1}{2} \sum_{i,j} H^{e-e}(\mathbf{r}_i, \mathbf{r}_j), \quad (14)$$

where  $H_{1e}$  is the single electron Hamiltonian:

$$H_{1e}(\mathbf{r}_i) = \frac{\mathbf{p}^2}{2m} + V_0(\mathbf{r}_i). \quad (15)$$

In which the  $V_0(\mathbf{r})$  is interaction between electron and ions. The Coulomb interaction between two electrons can be described by:

$$H^{e-e}(\mathbf{r}_i, \mathbf{r}_j) = V_{e-e}(\mathbf{r}_i, \mathbf{r}_j) = \frac{1}{4\pi\epsilon\epsilon_0} \frac{e^2}{|\mathbf{r}_i - \mathbf{r}_j|}, \quad (16)$$

in which the  $\epsilon_0$  is the vacuum permittivity,  $\epsilon$  is relative permittivity. In the present of an external electromagnetic field, the Hamiltonian for an electron in the independent electron approximation takes the form:

$$H_{1e} = \frac{(\mathbf{p} + e\mathbf{A})^2}{2m} + V_0(\mathbf{r}) - e\phi, \quad (17)$$

in which,  $\mathbf{A}(\mathbf{r}, t)$  is vector potential and  $\phi(\mathbf{r}, t)$  is scalar potential. With  $\mathbf{p} = -i\hbar\nabla$ , we expand  $(\mathbf{p} + e\mathbf{A})^2 = \mathbf{p}^2 + 2e\mathbf{A}\mathbf{p} + ei\hbar\nabla(\mathbf{A}) + (e\mathbf{A})^2$ . We have  $\nabla \cdot (\mathbf{A}) = 0$  due to Coulomb gauge, so the Eq. (17) becomes

$$H_{1e} = H_{1e}^0 + \frac{e}{m} \mathbf{A} \cdot \mathbf{p} + \frac{e^2 \mathbf{A}^2}{2m} - e\phi, \quad (18)$$

where the  $H_{1e}^0$  is stationary Hamiltonian of a single electron particle:

$$H_{1e}^0 = \frac{\mathbf{p}^2}{2m} + V_0(\mathbf{r}), \quad (19)$$

the rest in Eq. (18) shall be defined as the light-matter interaction Hamiltonian  $H_{1e}^{e-L}$ :

$$H_{1e}^{e-L} = \frac{e}{m} \mathbf{A} \cdot \mathbf{p} - e\phi + \frac{e^2 \mathbf{A}^2}{2m}. \quad (20)$$

When we choose gauge  $\phi = 0$ , the electromagnetic field's potential relation between  $\mathbf{A}$  and  $\phi$  becomes:

$$\mathbf{E} = -\nabla\phi - \frac{\partial\mathbf{A}}{\partial t} = -\frac{\partial\mathbf{A}}{\partial t}, \quad (21)$$

$$\mathbf{A}(\mathbf{r}, t) = -\int_{-\infty}^t dt' \mathbf{E}(\mathbf{r}, t'). \quad (22)$$



Substituting  $\phi = 0$  into Eq. (18),

$$H_{1e}^{VG} = H_{1e}^0 + \frac{e}{m} \mathbf{A} \cdot \mathbf{p} + \frac{e^2 \mathbf{A}^2}{2m}. \quad (23)$$

From the definition of the velocity operator  $\mathbf{v} = \frac{i}{\hbar} [H_{1e}, \mathbf{r}] = \frac{\mathbf{p} + e\mathbf{A}}{m}$ ,  $H_{1e}^{VG}$  can be written in the form

$$H_{1e}^{VG} = H_{1e}^0 + e\mathbf{A} \cdot \mathbf{v} - \frac{e^2 A^2}{2m}. \quad (24)$$

In velocity gauge, the light-matter interaction Hamiltonian (20) have the form:

$$H_{1e}^{e-L} = \frac{e}{m} \mathbf{A} \cdot \mathbf{p} + \frac{e^2 A^2}{2m}. \quad (25)$$

Combining Eqs. (19), (16), and (25), we obtain the many-body Hamiltonian describing the system of electrons interacting with an external electromagnetic field:

$$H = \sum_i H_{1e}^0(\mathbf{r}_i) + \sum_i H_{1e}^{e-L}(\mathbf{r}_i, t) + \frac{1}{2} \sum_{\mathbf{r}_i, \mathbf{r}_j} H^{e-e}(\mathbf{r}_i, \mathbf{r}_j). \quad (26)$$

### 2.3.2 Second Quantization Hamiltonian

From Eq. (26), the second quantization Hamiltonian in Bloch basis  $\{|\psi_{\lambda\mathbf{k}}\rangle\}$  has the form:

$$\begin{aligned} \hat{H} &= \hat{H}^0 + \hat{H}^{e-L} + \hat{H}^{e-e}, \\ \hat{H}^0 &= \sum_{\lambda\lambda'\mathbf{k}\mathbf{k}'} \langle \psi_{\lambda\mathbf{k}} | H_{1e}^0(\mathbf{r}) | \psi_{\lambda'\mathbf{k}'} \rangle c_{\lambda\mathbf{k}}^\dagger c_{\lambda'\mathbf{k}'}, \\ \hat{H}^{e-L} &= \sum_{\lambda\lambda'\mathbf{k}\mathbf{k}'} \langle \psi_{\lambda\mathbf{k}} | H^{e-L}(\mathbf{r}) | \psi_{\lambda'\mathbf{k}'} \rangle c_{\lambda\mathbf{k}}^\dagger c_{\lambda'\mathbf{k}'}, \\ \hat{H}^{e-e} &= \frac{1}{2} \sum_{\mathbf{k}, \mathbf{k}', \mathbf{q}} \sum_{\alpha\beta\gamma\delta} \langle \psi_{\alpha\mathbf{k} + \mathbf{q}} \psi_{\beta\mathbf{k}' - \mathbf{q}} | V_{e-e} | \psi_{\gamma\mathbf{k}'} \psi_{\delta\mathbf{k}} \rangle c_{\alpha, \mathbf{k} + \mathbf{q}}^\dagger c_{\beta, \mathbf{k}' - \mathbf{q}}^\dagger c_{\gamma, \mathbf{k}} c_{\delta, \mathbf{k}'}, \end{aligned} \quad (27)$$

in which the basis is orthonormal:  $\langle \psi_{\lambda\mathbf{k}} | \psi_{\lambda'\mathbf{k}'} \rangle = \delta_{\lambda\lambda'} \delta_{\mathbf{k}\mathbf{k}'}$ , and the creation and annihilation operators satisfy the anti-commutator relations:

$$\{c_{\lambda, \mathbf{k}}, c_{\lambda', \mathbf{k}'}\} = \{c_{\lambda, \mathbf{k}}^\dagger, c_{\lambda', \mathbf{k}'}^\dagger\} = 0, \quad \{c_{\lambda, \mathbf{k}}, c_{\lambda', \mathbf{k}'}^\dagger\} = \delta_{\lambda\lambda'} \delta_{\mathbf{k}\mathbf{k}'}. \quad (28)$$

If we choose the basis is a set of eigenvectors of  $H_{1e}^0$  then  $H^0$  becomes:

$$\hat{H}^0 = \sum_{\lambda\mathbf{k}} \varepsilon_\lambda(\mathbf{k}) c_{\lambda\mathbf{k}}^\dagger c_{\lambda\mathbf{k}}. \quad (29)$$

It is worth noting that the eigenvector of  $H_{1e}^0$  does not satisfy the orthonormality in general but only satisfies it if  $\mathbf{k} \approx \mathbf{k}'$ . In VG, the elements of interaction Hamiltonian matrix  $\langle \psi_{\lambda\mathbf{k}} | H^{e-L}(\mathbf{r}, t) | \psi_{\lambda'\mathbf{k}'} \rangle$  is:

$$\begin{aligned} \langle \psi_{\lambda\mathbf{k}} | H^{e-L}(\mathbf{r}, t) | \psi_{\lambda'\mathbf{k}'} \rangle &= \langle \psi_{\lambda\mathbf{k}} | \frac{e}{m} \mathbf{A}(\mathbf{r}, t) \cdot \mathbf{p} | \psi_{\lambda'\mathbf{k}'} \rangle + \frac{e^2 A^2}{2m} \delta_{\lambda\lambda'} \delta_{\mathbf{k}\mathbf{k}'} \\ &\approx \frac{e}{m} \mathbf{A}(t) \cdot \langle \psi_{\lambda\mathbf{k}} | \mathbf{p} | \psi_{\lambda'\mathbf{k}'} \rangle + \frac{e^2 A^2}{2m} \delta_{\lambda\lambda'} \delta_{\mathbf{k}\mathbf{k}'}, \end{aligned} \quad (30)$$

where

$$\begin{aligned}
\langle \psi_{\lambda \mathbf{k}} | \mathbf{p} | \psi_{\lambda' \mathbf{k}'} \rangle &= \int \frac{d^3 r}{V} e^{-i \mathbf{k} \cdot \mathbf{r}} u_{\lambda \mathbf{k}}^*(\mathbf{r}) \hat{\mathbf{p}} (e^{i \mathbf{k}' \cdot \mathbf{r}} u_{\lambda' \mathbf{k}'}(\mathbf{r})) \\
&= \int \frac{d^3 r}{V} e^{i(\mathbf{k}' - \mathbf{k}) \cdot \mathbf{r}} u_{\lambda \mathbf{k}}^*(\mathbf{r}) (\hbar \mathbf{k} + \hat{\mathbf{p}}) u_{\lambda' \mathbf{k}'}(\mathbf{r}) \\
&= \frac{1}{N} \sum_i^N e^{i(\mathbf{k}' - \mathbf{k}) \mathbf{R}_i} \int_{V_{Cell}} \frac{d^3 r}{V_{Cell}} e^{i(\mathbf{k}' - \mathbf{k}) \cdot \mathbf{r}} u_{\lambda \mathbf{k}}^*(\mathbf{r}) (\hbar \mathbf{k} + \hat{\mathbf{p}}) u_{\lambda' \mathbf{k}'}(\mathbf{r}). \tag{31}
\end{aligned}$$

We include the Long-wavelength approximation  $\mathbf{k}', \mathbf{k} \ll \frac{2\pi}{a}$  to have:

$$\begin{aligned}
\langle \psi_{\lambda \mathbf{k}} | \mathbf{p} | \psi_{\lambda' \mathbf{k}'} \rangle &\approx \frac{1}{N} \sum_i^N e^{i(\mathbf{k}' - \mathbf{k}) \mathbf{R}_i} \int_{V_{Cell}} \frac{d^3 r}{V_{Cell}} u_{\lambda \mathbf{k}}^*(\mathbf{r}) (\hbar \mathbf{k}' + \hat{\mathbf{p}}) u_{\lambda' \mathbf{k}'}(\mathbf{r}) \\
&\approx \frac{1}{N} \sum_i^N e^{i(\mathbf{k}' - \mathbf{k}) \mathbf{R}_i} (\hbar \mathbf{k}' \langle u_{\lambda \mathbf{k}} | u_{\lambda' \mathbf{k}'} \rangle + \langle u_{\lambda \mathbf{k}} | \hat{\mathbf{p}} | u_{\lambda' \mathbf{k}'} \rangle), \tag{32}
\end{aligned}$$

using relation  $\sum_i^N e^{i(\mathbf{k}' - \mathbf{k}) \mathbf{R}_i} = N \delta_{\mathbf{k}', \mathbf{k}}$ . Eq. (32) becomes

$$\langle \psi_{\lambda \mathbf{k}} | \mathbf{p} | \psi_{\lambda' \mathbf{k}'} \rangle \approx (\mathbf{p}_{\lambda \lambda'}(\mathbf{k}) + \hbar \mathbf{k} \delta_{\lambda \lambda'}) \delta_{\mathbf{k}, \mathbf{k}'}. \tag{33}$$

In which,

$$\mathbf{p}_{\lambda \lambda'}(\mathbf{k}) = \langle u_{\lambda \mathbf{k}} | \mathbf{p} | u_{\lambda' \mathbf{k}} \rangle. \tag{34}$$

It depends on whether the momentum matrix elements  $\mathbf{p}_{\lambda \lambda'}(\mathbf{k})$  are equal to 0 or not, to determine whether the transition between  $\lambda$  and  $\lambda'$  at  $\mathbf{k}$  is allowed. Using  $H_{1e}^0(\mathbf{k}) = e^{-i \mathbf{k} \mathbf{r}} H_{1e}^0 e^{i \mathbf{k} \mathbf{r}}$  and the relation:  $[H_{1e}^0, \mathbf{r}] = -i \frac{\hbar}{m} \mathbf{p}$  to have

$$\mathbf{p}_{\lambda \lambda'}(\mathbf{k}) = \frac{m}{\hbar} \langle u_{\lambda \mathbf{k}} | \nabla_{\mathbf{k}} H_{1e}^0(\mathbf{k}) | u_{\lambda' \mathbf{k}} \rangle. \tag{35}$$

Eq. (35) enables us to numerically calculate the momentum matrix elements at discrete  $\mathbf{k}$ -points. Therefore, the light-matter interaction part of the second quantization Hamiltonian takes the following form:

$$\hat{H}^{e-L} = \frac{e}{m} \mathbf{A}(t) \cdot \sum_{\lambda \lambda' \mathbf{k}} \mathbf{p}_{\lambda \lambda'}(\mathbf{k}) c_{\lambda \mathbf{k}}^\dagger c_{\lambda' \mathbf{k}} + \left( \hbar \mathbf{k} + \frac{e^2 \mathbf{A}^2}{2m} \right) \sum_{\lambda \mathbf{k}} c_{\lambda \mathbf{k}}^\dagger c_{\lambda \mathbf{k}}. \tag{36}$$

The  $H^{e-e}$  derivation is presented in Appendix A. Thus, the many-body Hamiltonian in second quantization in VG has the form:

$$\begin{aligned}
\hat{H} &= \hat{H}_{1e}^0 + \hat{H}^{e-e} + \hat{H}^{e-L} \\
&= \sum_{\lambda \mathbf{k}} \varepsilon_{\mathbf{k}} c_{\lambda \mathbf{k}}^\dagger c_{\lambda \mathbf{k}} \\
&\quad + \frac{1}{2} \sum_{\mathbf{k}, \mathbf{k}', \mathbf{q}} \sum_{\alpha \beta \gamma \delta} W_{\mathbf{k}, \mathbf{k}', \mathbf{q}}^{\alpha \beta \gamma \delta} c_{\alpha, \mathbf{k} + \mathbf{q}}^\dagger c_{\beta, \mathbf{k} - \mathbf{q}}^\dagger c_{\gamma, \mathbf{k}} c_{\delta, \mathbf{k}'} \\
&\quad + \frac{e}{m} \mathbf{A}(t) \cdot \sum_{\lambda \lambda' \mathbf{k}} \mathbf{p}_{\lambda \lambda'}(\mathbf{k}) c_{\lambda \mathbf{k}}^\dagger c_{\lambda' \mathbf{k}} + \left( \hbar \mathbf{k} + \frac{e^2 \mathbf{A}^2}{2m} \right) \sum_{\lambda \mathbf{k}} c_{\lambda \mathbf{k}}^\dagger c_{\lambda \mathbf{k}}, \tag{37}
\end{aligned}$$

where the Coulomb interaction matrix elements are:

$$W_{\mathbf{k},\mathbf{k}',\mathbf{q}}^{\alpha\beta\gamma\delta} = V_{e-e}(\mathbf{q}) \langle u_{\alpha\mathbf{k}+\mathbf{q}} | u_{\delta\mathbf{k}} \rangle \langle u_{\beta\mathbf{k}'-\mathbf{q}} | u_{\gamma\mathbf{k}'} \rangle, \quad (38)$$

with the 2-D Coulomb interaction in momentum space:

$$V_{e-e}(\mathbf{q}) = \frac{e^2}{2\varepsilon\varepsilon_0 L^2} \frac{1}{|\mathbf{q}|}. \quad (39)$$

## 2.4 Semiconductor Bloch Equation

With definition of density matrix elements,

$$\rho_{\lambda\lambda'}(\mathbf{k}) = \langle c_{\lambda'\mathbf{k}}^\dagger c_{\lambda\mathbf{k}} \rangle, \quad (40)$$

We use the equation of motion in Heisenberg picture for operator  $c_{\lambda'\mathbf{k}}^\dagger c_{\lambda\mathbf{k}}$  and take its expectation value to have:

$$\frac{d}{dt} \langle c_{\lambda'\mathbf{k}}^\dagger c_{\lambda\mathbf{k}} \rangle = \frac{i}{\hbar} \langle [H, c_{\lambda'\mathbf{k}}^\dagger c_{\lambda\mathbf{k}}] \rangle. \quad (41)$$

Through the derivation in Appendix B, we have obtained the Semiconductor Bloch Equation(s) with Coulomb interaction in the Hartree-Fock approximation:

$$\begin{aligned} \frac{d}{dt} \rho_{\lambda\lambda'}(\mathbf{k}) = & -\frac{i}{\hbar} (\varepsilon_\lambda(\mathbf{k}) - \varepsilon_{\lambda'}(\mathbf{k})) \rho_{\lambda\lambda'}(\mathbf{k}) - \frac{ie}{\hbar m} \mathbf{A}(t) \sum_{\mu} [\mathbf{p}_{\lambda\mu}(\mathbf{k}) \rho_{\mu\lambda'}(\mathbf{k}) - \rho_{\lambda\mu}(\mathbf{k}) \mathbf{p}_{\mu\lambda'}(\mathbf{k})] \\ & + \frac{i}{\hbar} [\Omega_{\lambda\mu}(\mathbf{k}) \rho_{\mu\lambda'}(\mathbf{k}) - \rho_{\lambda\mu}(\mathbf{k}) \Omega_{\mu\lambda'}(\mathbf{k})] + \left. \frac{d}{dt} \rho_{\lambda\lambda'}(\mathbf{k}) \right|_{\text{scat.}}, \end{aligned} \quad (42)$$

where

$$\Omega_{\mu\nu}(\mathbf{k}) = \sum_{\alpha\beta\mathbf{q}} W_{\mathbf{k},\mathbf{k}+\mathbf{q},\mathbf{q}}^{\alpha\mu\beta\nu} \rho_{\alpha\beta}(\mathbf{k} + \mathbf{q}). \quad (43)$$

The term "interband polarization" describes the decay of quantum coherence. A common and generally accurate approximation is to use the dephasing time parameter  $T_2$ , also known as the transverse relaxation time. This simple approximation is limited by nonlinear and non-Markovian effects, which can be ignored in this work. Therefore,

$$\left( \left. \frac{d}{dt} \rho(\mathbf{k}) \right|_{\text{scat.}} \right)_{\lambda\lambda'} \approx -\frac{\rho_{\lambda\lambda'}(\mathbf{k})}{T_2} \quad \forall \lambda \neq \lambda'. \quad (44)$$

Including Eq. (44) into Eq. (42), we obtain the Semiconductor Bloch Equations<sup>25</sup>:

$$\begin{aligned} \frac{d}{dt} \rho_{\lambda\lambda'}(\mathbf{k}) = & -\frac{i}{\hbar} (\varepsilon_\lambda(\mathbf{k}) - \varepsilon_{\lambda'}(\mathbf{k})) \rho_{\lambda\lambda'}(\mathbf{k}) - \frac{ie}{\hbar m} \mathbf{A}(t) \sum_{\mu} (\mathbf{p}_{\lambda\mu}(\mathbf{k}) \rho_{\mu\lambda'}(\mathbf{k}) - \rho_{\lambda\mu}(\mathbf{k}) \mathbf{p}_{\mu\lambda'}(\mathbf{k})) \\ & + \frac{i}{\hbar} (\Omega_{\lambda\mu}(\mathbf{k}) \rho_{\mu\lambda'}(\mathbf{k}) - \rho_{\lambda\mu}(\mathbf{k}) \Omega_{\mu\lambda'}(\mathbf{k})) - \frac{1}{T_2} \rho_{\lambda\lambda'}(\mathbf{k}) (1 - \delta_{\lambda\lambda'}), \end{aligned} \quad (45)$$

where

$$\Omega_{\mu\nu}(\mathbf{k}) = \sum_{\alpha\beta\mathbf{q}} W_{\mathbf{k},\mathbf{k}+\mathbf{q},\mathbf{q}}^{\alpha\mu\beta\nu} \rho_{\alpha\beta}(\mathbf{k} + \mathbf{q}). \quad (46)$$

## 2.5 Polarization Density

Polarization density is calculated from the trace of dipole and density matrix multiplication

$$\mathbf{P}(t) = \frac{e}{L^2} \sum_{\mathbf{k}} \text{Tr} \left[ \vec{\xi}(\mathbf{k}) \rho(\mathbf{k}, t) \right] = \frac{e}{L^2} \sum_{\lambda\lambda'\mathbf{k}} \vec{\xi}_{\lambda\lambda'}(\mathbf{k}) \rho_{\lambda'\lambda}(\mathbf{k}, t). \quad (47)$$

Taking the sum over all  $\mathbf{k}$ -points in the first BZ in 2D  $\mathbf{k}$ -grid through the integral

$$\sum_{\mathbf{k}} \dots \rightarrow \frac{L^2}{(2\pi)^2} \int_{\text{BZ}} d^2k \dots \quad (48)$$

Including it into polarization density Eq. (47) to have:

$$\mathbf{P}(t) = \frac{e}{L^2} \sum_{\mathbf{k}} \text{Tr} \left[ \vec{\xi}(\mathbf{k}) \rho(\mathbf{k}, t) \right] = \frac{1}{(2\pi)^2} \sum_{\lambda\lambda'} \int \vec{\xi}_{\lambda\lambda'}(\mathbf{k}) \rho_{\lambda'\lambda}(\mathbf{k}, t) d\mathbf{k}, \quad (49)$$

in which the dipole  $\vec{\xi}_{\lambda\lambda'}(\mathbf{k})$  can be calculated through  $\mathbf{p}_{\lambda\lambda'}(\mathbf{k})$  (derived in appendix C):

$$\vec{\xi}_{\lambda\lambda'}(\mathbf{k}) = -\frac{i\hbar}{m} \frac{\mathbf{p}_{\lambda\lambda'}(\mathbf{k})}{\varepsilon_{\lambda}(\mathbf{k}) - \varepsilon_{\lambda'}(\mathbf{k})}. \quad (50)$$

The numerical result of Eq. (49) will be obtained by using the Riemann sum integral.

### 3 Numerical Methods

#### 3.1 Numerical Sum Over k-Space

Monolayer TMD's actual lattice, denoted as  $MX_2$ , possesses the  $D_3h$  point-group symmetry, which is illustrated in Fig. 1. The 2D first Brillouin zone takes on the shape of a hexagon. This study concentrates on the linear abortion spectrum, a feature that relies heavily on the k-point with the direct band gap of this material. To numerical calculate the Eq. (49), we need to take numerical integral over the first BZ, which is inconvenient when working with the hexagon shape. Furthermore, a direct band gap is observed at the K and K' points in the first BZ, as depicted in Fig. (2). There are three K and three K' points situated at the edge of the first BZ as shown in fig. 3, with each point being shared between three BZ. Consequently, we need to calculate the average numerical position by adding up the positions and then dividing by the number of points, which can pose further challenges for the many-body problems we are addressing.

To address this, we introduce the use of the rhombus primitive cell, as shown in Fig. 3. This cell is constructed from 4 M-points located between K and K' on the edge of the hexagon, enabling us to focus on the properties of K and K' points both individually and in pairs.

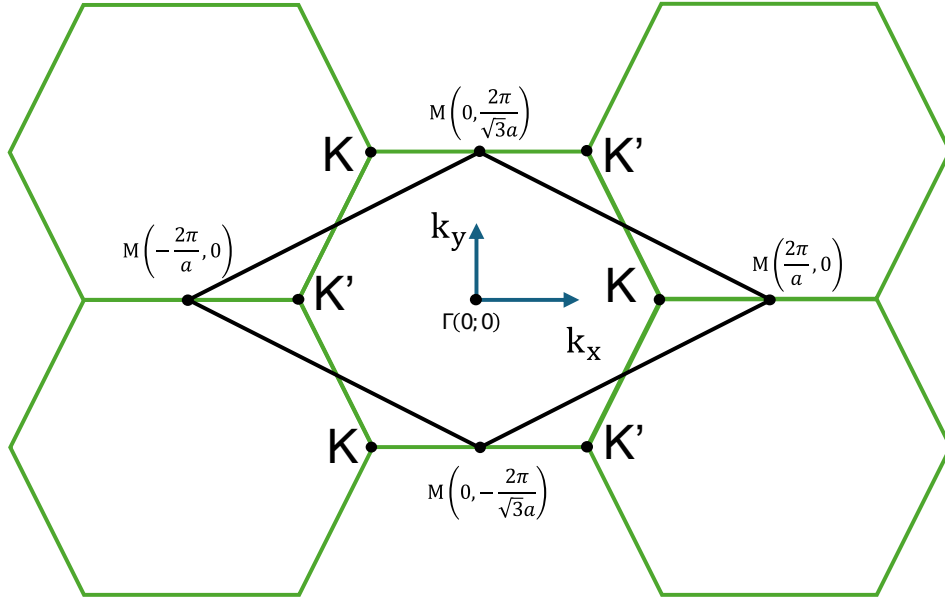


Figure 3: Rhombus primitive unit cell constructed through four M-points, which has the same area as the first Brillouin zone (the green Hexagon with six corners at "K-point" and "K'-point")

In order to establish a new coordinate system, we will utilize the two unit vectors located at the left corner of the rhombus  $u_1 = (2\pi/3a, 2\pi/\sqrt{3}a)$  and  $u_2 = (2\pi/3a, -2\pi/\sqrt{3}a)$  as shown in Fig. 4, which will be reference to as the "Rhombus basis" hereinafter. Consider a point  $\mathbf{P}$ ,

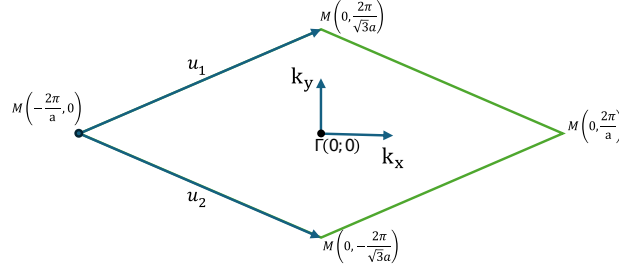


Figure 4: New basis Based on the rhombus unit vectors

which have coordinate  $(v_1, v_2)$  in rhombus basis and coordinate  $(k_x, k_y)$  in rectangular basis. These coordinate have the relation through the transformation:

$$\begin{pmatrix} k_x \\ k_y \end{pmatrix} = \frac{2\pi}{a} \begin{pmatrix} 1 & 1 \\ \frac{1}{\sqrt{3}} & -\frac{1}{\sqrt{3}} \end{pmatrix} \begin{pmatrix} v_1 \\ v_2 \end{pmatrix} - \begin{pmatrix} \frac{2\pi}{a} \\ 0 \end{pmatrix}, \quad \begin{pmatrix} v_1 \\ v_2 \end{pmatrix} = \frac{a}{4\pi} \begin{pmatrix} 1 & \sqrt{3} \\ 1 & -\sqrt{3} \end{pmatrix} \begin{pmatrix} k_x \\ k_y \end{pmatrix} + \begin{pmatrix} 1/2 \\ 1/2 \end{pmatrix}, \quad (51)$$

Since the  $v_1, v_2$  is a continuous variable, we need to convert it into discrete coordinates in order to proceed with a numerical solution. To do this, we divide the vectors  $u_1$  and  $u_2$  into  $n$  equal segments, which are then labeled as  $n_1$  and  $n_2$ , respectively. We discrete the continuous coordinate  $(v_1, v_2)$  in term of  $(n_1, n_2)$ :

$$\begin{cases} v_1 = n_1 \frac{u_1}{n} \\ v_2 = n_2 \frac{u_2}{n} \end{cases}, n_1, n_2 \in \{0, 1, \dots, n\}.$$

### 3.2 Cut-off K-point Technique

In our research, we are focusing on the transition between the valence and conduction bands around the K and K' points. We achieve this by using a small-intensity electric field and limiting the photon energy to around the band gap energy  $E_{gap}$ . However, the calculation of the Coulomb interaction for every point in the rhombus with other points all over the rhombus is not efficient in terms of time cost, and convergence. As demonstrated in the 2-D Coulomb interaction Eq. (39), the Coulomb potential is inversely proportional to the distance between two points in k-space. To address this issue, we are introducing a technique to limit the points taken into account in the Coulomb interaction part.

In the diagram shown in Fig. 5, a circle is drawn around the K' point with a radius of  $k_{cut.}$ . When calculating the Eq. (45) at a k-point, if this k-point is outside the circle, we use

$$\Omega_{\mu\nu}(\mathbf{k}) = 0 \quad \forall \mu, \nu.$$

When dealing with k-point inside the circle, we only consider interactions with other points inside the circle. This reduces the computational load significantly. In a 2-dimensional system,

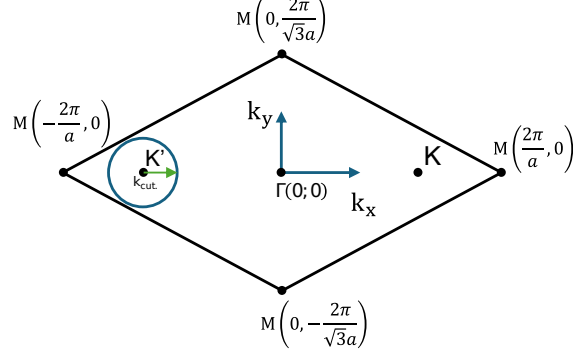


Figure 5: k-radius show the cutoff circle around  $K'$  points

each doubling of k-points results in a 32-fold increase in simulation time (we calculate on both  $K$  and  $K'$ ). However, by focusing around the  $K/K'$  point and reducing the number of k-points, the time cost only increases by approximately 8 to 10 times.

In summary, we approximate the Coulomb interaction matrix elements:

$$W_{\mathbf{k}, \mathbf{k}', \mathbf{q}}^{\alpha\mu\beta\nu} \approx W_{\mathbf{k}, \mathbf{k}', \mathbf{q}}^{\alpha\mu\beta\nu} \theta(k_{cut.} - |\mathbf{k} - \mathbf{k}_{K'}|) \theta(k_{cut.} - |\mathbf{k}' - \mathbf{k}_{K'}|).$$

Where  $\theta(k)$  represents the Heaviside function, the Coulomb interaction is excluded if either point is outside the circle. The same process applies for the  $K$  point.

### 3.3 Absorption and Electromagnetic Field

The linear absorption spectrum is determined by<sup>25</sup>

$$\alpha(\omega) \propto \text{Im} \left\{ \frac{P(\omega)}{E(\omega)} \right\}. \quad (52)$$

In which  $\mathbf{P}(\omega) = \int_{-\infty}^{\infty} \mathbf{P}(t) e^{i\omega t} dt$  and  $\mathbf{E}(\omega) = \int_{-\infty}^{\infty} \mathbf{E}(t) e^{i\omega t} dt$  are the Fourier transform for polarization density and electric field. These integral can be approximated using a Riemann sum with the cut-off point by using condition  $\mathbf{E}(t_{cutoff}) \lesssim 10^{-6} |\max \mathbf{E}(t)|$  and  $\mathbf{P}(t_{cutoff}) \lesssim 10^{-6} |\max \mathbf{P}(t)|$ . In this work, we are using the electric field in form:

$$\mathbf{E}(t) = E_0 e^{-\frac{t^2}{\tau_L^2}} (\cos(\omega_0 t), 0), \quad (53)$$

with the  $E_0$  is the maximal amplitude,  $\hbar\omega_0 = E_{\text{gap}}$ ,  $\tau_L$  is the duration of the Gaussian envelope, and  $t$  is time, all will be calculated in SI units. The  $E_x(t)$  and its Fourier transform shape are shown in Fig. 6.

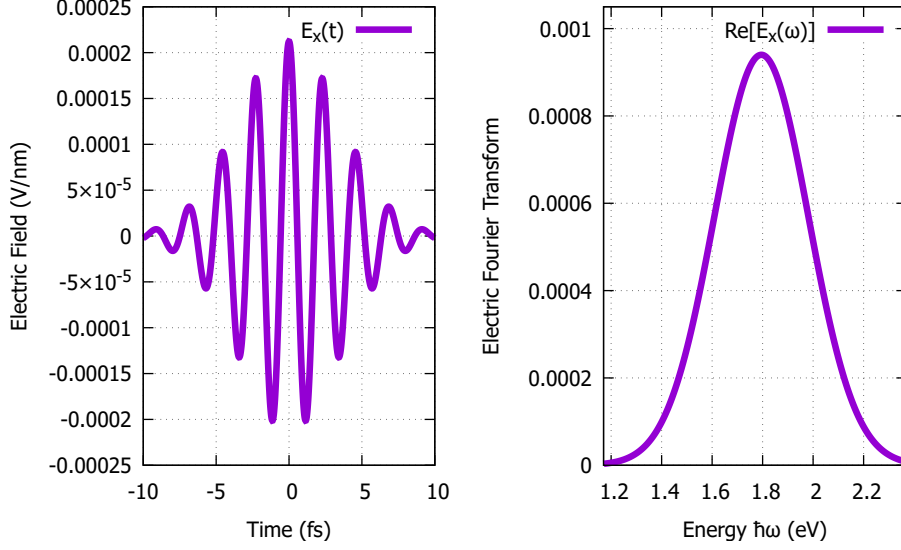


Figure 6: Electric field on Ox direction and its Fourier Transform

## 4 Results and Discussion

In the previous study<sup>12</sup>, the absorption spectrum of MoS<sub>2</sub> at  $T = 5K$  was measured and presented in Fig. 7. The results revealed two exciton resonances labeled as A and B, which were observed at energy levels of 1.9 and 2.1 eV, respectively. Additionally, a small trion peak was observed before the A peak. The splitting between the exciton and trion absorption peaks was approximately 34 meV at 5K.

When solving the SBE numerically, we utilize the external electric field as follows:  $E_0 = \frac{3}{\sqrt{2}} \times 10^3$  V/cm,  $\hbar\omega_0 = E_{\text{gap}} = 1.77$  eV, time step  $\Delta t = 0.02$  fs,  $T_2 = 20$  fs, and cutoff the Coulomb interaction at  $3.0 \text{ nm}^{-1}$  around K and K' points to simplify the calculation. By simulating with the given parameters, we observe that the density of electrons in the conduction bands after the external field passes is relatively small compared to the initial electron density in the valence bands ( $1.10^7 \text{ cm}^{-2} \ll 1.10^{11} \text{ cm}^{-2}$ ), which confirms our discussion on the neglect of electron-electron scattering in Eq. (45). We perform Fourier transforms of energies from above and below the band gap by 1 eV. There are three main parameters we can adjust to obtain results that agree with recent measurement or predict future measurements: relative dielectric  $\varepsilon$ , dephasing time  $T_2$ , and the number of k points on the k grid.

In Fig. 8, our results for calculating the absorption spectrum with LDA parameters are presented, where the dielectric constant is  $\varepsilon = 2.5$  with difference  $T_2$ . As  $T_2$  increases, two main peaks become clearer at 1.528 and 1.640 eV, indicating a binding energy of approximately 0.25 eV.

We present our results for calculating the absorption spectrum using the LDA parameter and the difference dielectric  $\varepsilon$  in Fig. 9. As the dielectric constant  $\varepsilon$  increases, two main peaks shift to the right, which can be used to determine the fitting value with the experiment, the



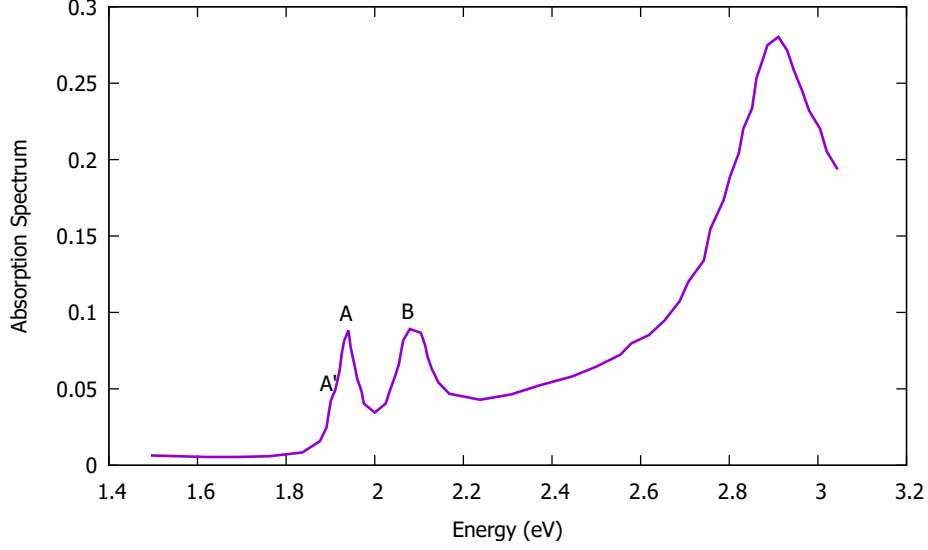


Figure 7: absorption spectrum of MoS<sub>2</sub> at  $T = 5K$  extracted from<sup>12</sup>, two exciton resonances labeled by A and B, and small trion peak labeled with A'.

exciton binding energy result vary on dielectric parameter  $\varepsilon$  shown in Tab. 2.

In Fig. 10, we present our numerical results with varying numbers of k-grid points, using a

$\varepsilon$	1.0	1.5	2.0	2.5
$E_{\text{bind.}}(eV)$	0.95	0.55	0.36	0.25

Table 2: Exciton binding energy with difference dielectric  $\varepsilon$

dielectric constant of  $\varepsilon = 2.5$  to demonstrate the convergence of the results. The calculations show well convergence when the value of  $nk$  increase from 60. To strike a balance between precision and time cost, we opt for  $nk = 60$  for the subsequent calculations.

With a small  $T_2$  of 15 *fs*, the results in Fig. 8 have already shown two main exciton peaks in comparison with the experimental results in Fig. 7. However, as the  $T_2$  increases at the cost of simulation time, we can see smaller exciton peaks in the absorption spectrum, as described in fig. 8. These A and B exciton resonances involve the conduction bands and two valence bands (split due to spin-orbit coupling) near the K and K' points, as shown in the band structure in Fig. 2, providing evidence for the good approximation of the transverse relaxation time  $T_2$ . In our results shown in Fig. 8 and the experiment by Zhang et al.<sup>12</sup> in Fig. 7, we observe that the energy peak does not align with the expected value for the dielectric constant  $\varepsilon = 2.5$ . As per the data in Fig. 7<sup>12</sup>, the exciton peaks are situated at 1.9 and 2.1 eV, while in our calculations, the two peaks are at 1.528 and 1.640 eV, indicating a binding energy of the exciton of about 0.25 eV. If we only consider the distance from the band gap, our result is smaller than some previous calculations predicting the binding

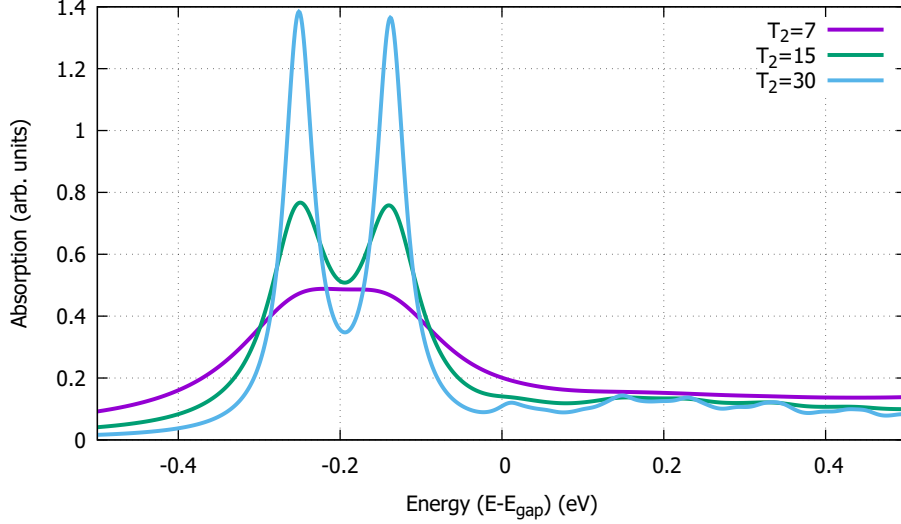


Figure 8: Absorption Spectrum with difference  $T_2$

energy between 0.5 eV to 1 eV<sup>13-16</sup>. This result agrees with more precise calculations and measurements<sup>11;12;26</sup>. The difference in band gap energy can be attributed to the use of DFT calculations in our model<sup>19</sup>. This model does not consider the band gap shift caused by the underlying layers and temperature variations in the experimental measurement. The absence of the trion peak in Fig. 8 in compare with Fig. 7 is due to the trion involving an interaction between three particles (2 holes and 1 electron for a positive trion, 1 hole and 2 electrons for a negative trion), which is not included in the Hartree-Fock approximation. To observe the trion peak, it is suggested to go beyond the HFA in established equations.

This model is effective and has advantages for calculation over BZ, but it also has disadvantages and requires denser k-grids for results to converge (as shown in Fig. 10) compared to DFT models or parabola approximation models. The bare Coulomb interaction works well in calculating the linear absorption spectrum, but for a more realistic case, the shield Coulomb interaction must be taken into account<sup>27;28</sup>, especially when we want to go beyond the small excitation limit. It's worth noting that the parameter  $T_2$  is proved to be a good approximation without requiring further techniques in showing two main exciton peaks and predicting other smaller peaks. However, for a more realistic representation, the  $T_2$  approximation can also be expanded in terms of electron-electron and electron-phonon scattering terms, which would provide a more comprehensive analysis of the system under consideration. Additionally, it is crucial to consider the implications of these findings in the context of practical applications and the broader theoretical framework.

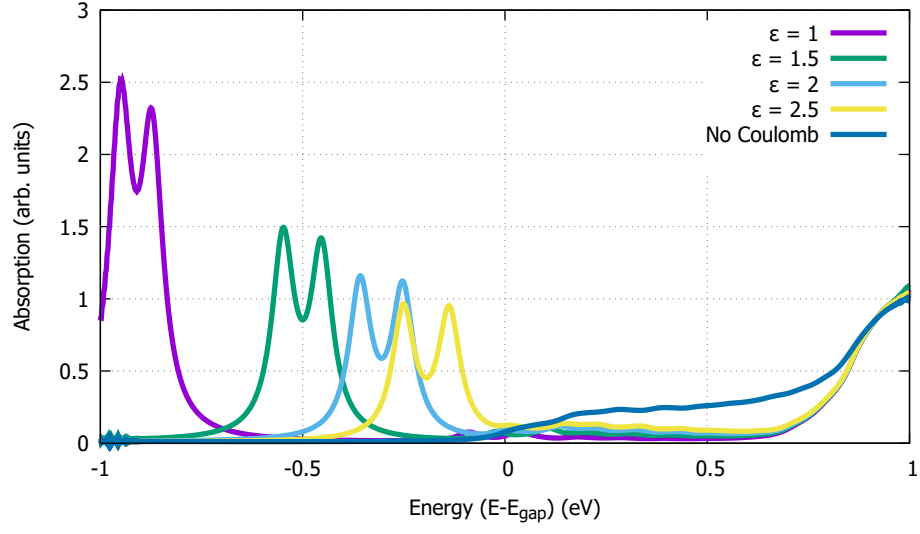


Figure 9: Absorption Spectrum with difference dielectric  $\varepsilon$  and without Coulomb interaction

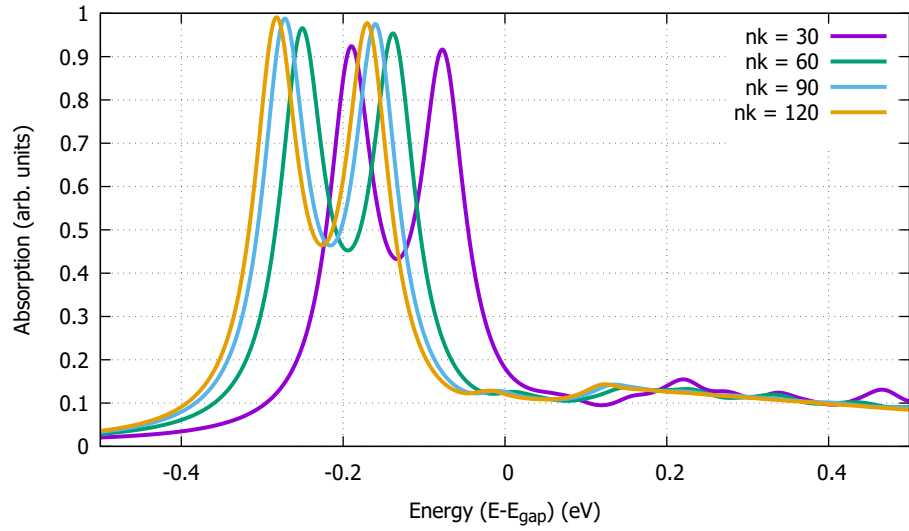


Figure 10: Absorption Spectrum with difference number of k-points

## 5 Conclusion and Further Research

In our research, we have calculated the linear absorption of monolayer MoS<sub>2</sub> using a tight-binding three-band model with spin-orbit coupling through semiconductor Bloch equations in Hartree-Fock approximation. We have varied three parameters to analyze their relation with the absorption spectrum and found that the results align with other calculations, indicating a significant binding energy up to two magnitude in comparison with other bulk semiconductors.

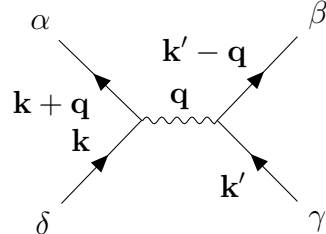
We have encountered some limitations, like the time-consuming process of enhancing the k-grid for better convergence and the discrepancy in the bandgap position as compared to experimental data. We also have observed that the bare Coulomb interaction might not be adequate for an accurate depiction and should be fine-tuned for better outcomes.

For further researches, we can utilize this three-band tight-binding model to calculate other optoelectronic phenomena affected by excitons, such as high harmonic generation (HHG), high-order sideband generation (HSG), and photovoltaic current. When calculating the photovoltaic effect, it's important to consider the influence of Coulomb interactions. Without the consideration of Coulomb interactions, only the shift current is apparent, as we've calculated the current tensors as per Ref.<sup>29</sup>. However, once we include the Coulomb interaction, the ballistic current becomes significant, and the shift tensor current is also affected. It's crucial to account for Coulomb interactions to obtain a realistic picture of the photovoltaic effect.

# Appendices

## A Coulomb matrix elements

The Coulomb matrix elements is



$$\begin{aligned}
 W_{\mathbf{k}, \mathbf{k}', \mathbf{q}}^{\alpha\beta\gamma\delta} &= \langle \psi_{\alpha\mathbf{k} + \mathbf{q}} \psi_{\beta\mathbf{k}' - \mathbf{q}} | V_{e-e} | \psi_{\gamma\mathbf{k}'} \psi_{\delta\mathbf{k}} \rangle = \\
 &= \int \frac{d^3r}{V} \int \frac{d^3r'}{V} e^{-i\mathbf{q}(\mathbf{r} - \mathbf{r}')} u_{\alpha\mathbf{k} + \mathbf{q}}^*(\mathbf{r}) u_{\beta\mathbf{k} - \mathbf{q}}^*(\mathbf{r}') V_{e-e}(\mathbf{r} - \mathbf{r}') u_{\gamma\mathbf{k}'}(\mathbf{r}') u_{\delta\mathbf{k}}(\mathbf{r}), \quad (54)
 \end{aligned}$$

with

$$V_{e-e}(\mathbf{r}) = \frac{e^2}{4\pi\epsilon\epsilon_0} \frac{1}{|\mathbf{r}|}, \quad (55)$$

we expand it using Fourier transform

$$\begin{aligned}
 V_{e-e}(\mathbf{q}) &= \int \frac{d^3\mathbf{r}}{V} V_{e-e}(\mathbf{r}) e^{-i\mathbf{q}\cdot\mathbf{r}} = \frac{e^2}{4\pi\epsilon\epsilon_0 V} \int d^3\mathbf{r} \frac{1}{|\mathbf{r}|} e^{-i\mathbf{q}\cdot\mathbf{r}} \\
 &= \frac{e^2}{4\pi\epsilon\epsilon_0 V} \int_0^\infty \int_0^{2\pi} \int_{-\pi}^\pi \frac{1}{r} r^2 e^{-iqr \cos(\theta)} dr d\varphi \cos(\theta) d\theta \\
 &= \frac{e^2}{2\epsilon\epsilon_0 V} \int_0^\infty \int_{-1}^1 r dr d\cos\theta e^{iqr \cos\theta} = -\frac{i}{q} \frac{e^2}{2\epsilon\epsilon_0 V} \int_0^\infty dr (e^{iqr} - e^{-iqr}) \\
 &= -\frac{i}{q} \frac{e^2}{2\epsilon\epsilon_0 V} \lim_{\gamma \rightarrow 0} \int_0^\infty dr (e^{iqr} - e^{-iqr}) e^{-\gamma r} \\
 &= \frac{e^2}{2\epsilon\epsilon_0 V} \lim_{\gamma \rightarrow 0} \left( \int_0^\infty \frac{e^{(iq-\gamma)r}}{iq-\gamma} dr - \int_0^\infty \frac{e^{-(iq+\gamma)r}}{iq+\gamma} dr \right) = \frac{e^2}{\epsilon\epsilon_0 V} \frac{1}{q^2}. \quad (56)
 \end{aligned}$$

Include (56) into (54) through reverse Fourier transform

$$\begin{aligned}
 V_{e-e}(\mathbf{r}) &= \sum_{\mathbf{q}} V_{e-e}(\mathbf{q}) e^{i\mathbf{q}\cdot\mathbf{r}} = \sum_{\mathbf{q}_{||}, \mathbf{q}_{\perp}} \frac{e^2}{\epsilon\epsilon_0 V} \frac{1}{\mathbf{q}_{||}^2 + q_{\perp}^2} e^{i\mathbf{q}_{||}\mathbf{r}_{||}} e^{iq_{\perp}r_{\perp}} \\
 &= \sum_{\mathbf{q}_{||}} \frac{1}{2\pi/L_z} \frac{e^2}{\epsilon\epsilon_0 V} e^{i\mathbf{q}_{||}\mathbf{r}_{||}} \int dq_{\perp} \frac{e^{iq_{\perp}r_{\perp}}}{\mathbf{q}_{||}^2 + q_{\perp}^2}, \quad (57)
 \end{aligned}$$

$$\begin{aligned}
 \bullet \int_{-\infty}^{\infty} dx \frac{e^{iax}}{a^2 + x^2} &= \oint dz \frac{e^{iaz}}{(z+ia)(z-ia)} = 2\pi i \text{Res}_{z=ia} \left[ \frac{e^{iaz}}{(z+ia)(z-ia)} \right] \\
 &= 2\pi i \lim_{z \rightarrow ia} \frac{e^{iaz}}{(z+ia)(z-ia)} (z-ia) = 2\pi i \frac{e^{-ax}}{2ia} = \frac{\pi e^{-ax}}{a} \quad (a > 0) \quad (58)
 \end{aligned}$$

$$\Rightarrow (57) = \sum_{\mathbf{q}_{||}} \frac{e^2}{2\epsilon\epsilon_0 V_{||}} e^{i\mathbf{q}_{||}\mathbf{r}_{||}} \frac{e^{-|\mathbf{q}_{||}||\mathbf{r}_{\perp}|}}{|\mathbf{q}_{||}|} = \sum_{\mathbf{q}_{||}} V_{||}^{2D}(\mathbf{q}_{||}, \mathbf{r}_{\perp}) e^{i\mathbf{q}_{||}\mathbf{r}_{||}} \quad (59)$$

$$\therefore V_{||}^{2D}(\mathbf{q}_{||}, z) = \frac{e^2}{2\varepsilon\varepsilon_0 V_{||}} \frac{e^{-|\mathbf{q}_{||}|z}}{|\mathbf{q}_{||}|}. \quad (60)$$

Include (60) back into (54) through (59) for 2D-case

$$\begin{aligned} W_{\mathbf{k}, \mathbf{k}', \mathbf{q}}^{\alpha\beta\gamma\delta} &= \int \int d\mathbf{r}_1 d\mathbf{r}_2 u_{\mathbf{k}_{||}+\mathbf{q}_{||}}^{\alpha\dagger}(\mathbf{r}_1) u_{\mathbf{k}'_{||}-\mathbf{q}_{||}}^{\beta\dagger}(\mathbf{r}_2) V^{3D}(\mathbf{r}_2 - \mathbf{r}_1) e^{i\mathbf{q}_{||}(\mathbf{r}_2 - \mathbf{r}_1)} u_{\mathbf{k}'_{||}}^{\gamma}(\mathbf{r}_2) u_{\mathbf{k}_{||}}^{\delta}(\mathbf{r}_1) \\ &= \frac{e^2}{2\varepsilon\varepsilon_0 V_{||}} \sum_{\mathbf{q}'_{||}} \int \int d\mathbf{r}_1 d\mathbf{r}_2 u_{\mathbf{k}_{||}+\mathbf{q}_{||}}^{\alpha\dagger}(\mathbf{r}_1) u_{\mathbf{k}'_{||}-\mathbf{q}_{||}}^{\beta\dagger}(\mathbf{r}_2) e^{i\mathbf{q}'_{||}(\mathbf{r}_2 - \mathbf{r}_1)} \frac{e^{-|\mathbf{q}'_{||}|z_2 - z_1}}{|\mathbf{q}'_{||}|} e^{i\mathbf{q}_{||}(\mathbf{r}_2 - \mathbf{r}_1)} u_{\mathbf{k}'_{||}}^{\gamma}(\mathbf{r}_2) u_{\mathbf{k}_{||}}^{\delta}(\mathbf{r}_1), \end{aligned} \quad (61)$$

We take the limit  $z_1, z_2 \rightarrow 0$ , therefore the  $W_{\mathbf{k}, \mathbf{k}', \mathbf{q}}^{\alpha\beta\gamma\delta}$  take the form:

$$W_{\mathbf{k}, \mathbf{k}', \mathbf{q}}^{\alpha\beta\gamma\delta} = \frac{e^2}{2\varepsilon\varepsilon_0 V_{||}} \sum_{\mathbf{q}} \frac{1}{|\mathbf{q}|} \langle u_{\mathbf{k}+\mathbf{q}}^{\alpha} | u_{\mathbf{k}}^{\delta} \rangle \langle u_{\mathbf{k}'-\mathbf{q}}^{\beta} | u_{\mathbf{k}'}^{\gamma} \rangle \quad (62)$$

## B Equation of Motion

We consider Hamiltonian (37), using Heisenberg motion equation part by part with creation and annihilation operator satisfies (28):

$$\begin{aligned}
[H_{1e}^0, c_{\alpha\mathbf{k}}^\dagger c_{\beta\mathbf{k}}] &= \sum_{\mathbf{k}'\lambda} \varepsilon_{\lambda,\mathbf{k}'} [c_{\lambda\mathbf{k}'}^\dagger c_{\lambda\mathbf{k}'}, c_{\alpha\mathbf{k}}^\dagger c_{\beta\mathbf{k}}] \\
&= \sum_{\mathbf{k}'\lambda} \varepsilon_{\lambda,\mathbf{k}'} (c_{\lambda\mathbf{k}'}^\dagger c_{\lambda\mathbf{k}'} c_{\alpha\mathbf{k}}^\dagger c_{\beta\mathbf{k}} - c_{\alpha\mathbf{k}}^\dagger c_{\beta\mathbf{k}} c_{\lambda\mathbf{k}'}^\dagger c_{\lambda\mathbf{k}'}) \\
&= \sum_{\mathbf{k}\lambda'} \varepsilon_{\lambda,\mathbf{k}} (c_{\lambda\mathbf{k}}^\dagger \delta_{\lambda\alpha} \delta_{\mathbf{k}\mathbf{k}'} c_{\beta\mathbf{k}} - c_{\lambda\mathbf{k}}^\dagger c_{\alpha\mathbf{k}}^\dagger c_{\lambda\mathbf{k}'} c_{\beta\mathbf{k}} - c_{\alpha\mathbf{k}}^\dagger \delta_{\beta\lambda} \delta_{\mathbf{k}\mathbf{k}'} c_{\lambda\mathbf{k}'} + c_{\alpha\mathbf{k}}^\dagger c_{\lambda\mathbf{k}'}^\dagger c_{\beta\mathbf{k}} c_{\lambda\mathbf{k}'}) \\
&= \sum_{\mathbf{k}\lambda'} \varepsilon_{\lambda,\mathbf{k}} (c_{\lambda\mathbf{k}}^\dagger \delta_{\lambda\alpha} \delta_{\mathbf{k}\mathbf{k}'} c_{\beta\mathbf{k}} - \cancel{c_{\alpha\mathbf{k}}^\dagger c_{\lambda\mathbf{k}'}^\dagger c_{\beta\mathbf{k}} c_{\lambda\mathbf{k}'}} - c_{\alpha\mathbf{k}}^\dagger \delta_{\beta\lambda} \delta_{\mathbf{k}\mathbf{k}'} c_{\lambda\mathbf{k}'} + \cancel{c_{\alpha\mathbf{k}}^\dagger c_{\lambda\mathbf{k}'}^\dagger c_{\beta\mathbf{k}} c_{\lambda\mathbf{k}'}}) \\
&= (\varepsilon_\alpha(\mathbf{k}) - \varepsilon_\beta(\mathbf{k})) c_{\alpha\mathbf{k}}^\dagger c_{\beta\mathbf{k}}
\end{aligned} \tag{63}$$

$$\begin{aligned}
[H^{e-L}, c_{\alpha\mathbf{k}}^\dagger c_{\beta\mathbf{k}}] &= \sum_{\lambda\lambda'\mathbf{k}'} \mathbf{p}_{\lambda\lambda'}(\mathbf{k}') [c_{\lambda\mathbf{k}'}^\dagger c_{\lambda'\mathbf{k}'}, c_{\alpha\mathbf{k}}^\dagger c_{\beta\mathbf{k}}] + \sum_{\lambda\mathbf{k}'} \left( \hbar\mathbf{k}' + \frac{e^2 A^2}{2m} \right) [\cancel{c_{\lambda\mathbf{k}'}^\dagger c_{\lambda\mathbf{k}'}, c_{\alpha\mathbf{k}}^\dagger c_{\beta\mathbf{k}}}] \\
&= \sum_{\lambda\lambda'\mathbf{k}'} \mathbf{p}_{\lambda\lambda'}(\mathbf{k}') (c_{\lambda\mathbf{k}'}^\dagger c_{\lambda'\mathbf{k}'} c_{\alpha\mathbf{k}}^\dagger c_{\beta\mathbf{k}} - c_{\alpha\mathbf{k}}^\dagger c_{\beta\mathbf{k}} c_{\lambda\mathbf{k}'}^\dagger c_{\lambda'\mathbf{k}'}) \\
&= \sum_{\lambda\lambda'\mathbf{k}'} \mathbf{p}_{\lambda\lambda'}(\mathbf{k}') (c_{\lambda\mathbf{k}'}^\dagger \delta_{\lambda'\alpha} \delta_{\mathbf{k}\mathbf{k}'} c_{\beta\mathbf{k}} - c_{\lambda\mathbf{k}'}^\dagger c_{\alpha\mathbf{k}}^\dagger c_{\lambda'\mathbf{k}'} c_{\beta\mathbf{k}} - c_{\alpha\mathbf{k}}^\dagger \delta_{\beta\lambda} \delta_{\mathbf{k}\mathbf{k}'} c_{\lambda'\mathbf{k}'} + c_{\alpha\mathbf{k}}^\dagger c_{\lambda\mathbf{k}'}^\dagger c_{\beta\mathbf{k}} c_{\lambda'\mathbf{k}'}) \\
&= \sum_{\lambda\lambda'\mathbf{k}'} \mathbf{p}_{\lambda\lambda'}(\mathbf{k}') (c_{\lambda\mathbf{k}'}^\dagger \delta_{\lambda'\alpha} \delta_{\mathbf{k}\mathbf{k}'} c_{\beta\mathbf{k}} - \cancel{c_{\lambda\mathbf{k}'}^\dagger c_{\alpha\mathbf{k}}^\dagger c_{\lambda'\mathbf{k}'} c_{\beta\mathbf{k}}} - c_{\alpha\mathbf{k}}^\dagger \delta_{\beta\lambda} \delta_{\mathbf{k}\mathbf{k}'} c_{\lambda'\mathbf{k}'} + \cancel{c_{\alpha\mathbf{k}}^\dagger c_{\lambda\mathbf{k}'}^\dagger c_{\beta\mathbf{k}} c_{\lambda'\mathbf{k}'}}) \\
&= \sum_{\lambda} (\mathbf{p}_{\lambda\alpha}(\mathbf{k}) c_{\lambda\mathbf{k}}^\dagger c_{\beta\mathbf{k}} - \mathbf{p}_{\beta\lambda}(\mathbf{k}) c_{\alpha\mathbf{k}}^\dagger c_{\lambda\mathbf{k}})
\end{aligned} \tag{64}$$

$$\begin{aligned}
[H^{Coulomb}, c_{\lambda\mathbf{k}''}^\dagger c_{\lambda'\mathbf{k}''}] &= \sum_{\mathbf{k},\mathbf{k}',\mathbf{q}} \sum_{\alpha\beta\gamma\delta} W_{\mathbf{k},\mathbf{k}',\mathbf{q}}^{\alpha\beta\gamma\delta} [c_{\alpha,\mathbf{k}+\mathbf{q}}^\dagger c_{\beta,\mathbf{k}'-\mathbf{q}}^\dagger c_{\gamma,\mathbf{k}\delta,\mathbf{k}'} c_{\lambda\mathbf{k}''}^\dagger c_{\lambda'\mathbf{k}''}] \\
&= \sum_{\mathbf{k},\mathbf{k}',\mathbf{q}} \sum_{\alpha\beta\gamma\delta} W_{\mathbf{k},\mathbf{k}',\mathbf{q}}^{\alpha\beta\gamma\delta} (c_{\alpha,\mathbf{k}+\mathbf{q}}^\dagger c_{\beta,\mathbf{k}'-\mathbf{q}}^\dagger c_{\gamma,\mathbf{k}\delta,\mathbf{k}'} c_{\lambda\mathbf{k}''}^\dagger c_{\lambda'\mathbf{k}''} - c_{\lambda\mathbf{k}''}^\dagger c_{\lambda'\mathbf{k}''} c_{\alpha,\mathbf{k}+\mathbf{q}}^\dagger c_{\beta,\mathbf{k}'-\mathbf{q}}^\dagger c_{\gamma,\mathbf{k}\delta,\mathbf{k}'}) \\
&\bullet \quad c_{\alpha,\mathbf{k}+\mathbf{q}}^\dagger c_{\beta,\mathbf{k}'-\mathbf{q}}^\dagger c_{\gamma,\mathbf{k}\delta,\mathbf{k}'} c_{\lambda\mathbf{k}''}^\dagger c_{\lambda'\mathbf{k}''} = c_{\alpha,\mathbf{k}+\mathbf{q}}^\dagger c_{\beta,\mathbf{k}'-\mathbf{q}}^\dagger c_{\gamma,\mathbf{k}\delta,\mathbf{k}'} \delta_{\lambda,\delta} \delta_{\mathbf{k}',\mathbf{k}''} c_{\lambda'\mathbf{k}''} - c_{\alpha,\mathbf{k}+\mathbf{q}}^\dagger c_{\beta,\mathbf{k}'-\mathbf{q}}^\dagger c_{\gamma,\mathbf{k}\delta,\mathbf{k}'} c_{\lambda\mathbf{k}''}^\dagger c_{\delta,\mathbf{k}'} c_{\lambda'\mathbf{k}''} \\
&= c_{\alpha,\mathbf{k}+\mathbf{q}}^\dagger c_{\beta,\mathbf{k}'-\mathbf{q}}^\dagger c_{\gamma,\mathbf{k}\delta,\mathbf{k}'} \delta_{\lambda,\delta} \delta_{\mathbf{k}',\mathbf{k}''} c_{\lambda'\mathbf{k}''} - c_{\alpha,\mathbf{k}+\mathbf{q}}^\dagger c_{\beta,\mathbf{k}'-\mathbf{q}}^\dagger \delta_{\lambda\gamma} \delta_{\mathbf{k}\mathbf{k}''} c_{\delta,\mathbf{k}'} c_{\lambda'\mathbf{k}''} + \cancel{c_{\alpha,\mathbf{k}+\mathbf{q}}^\dagger c_{\beta,\mathbf{k}'-\mathbf{q}}^\dagger c_{\lambda\mathbf{k}''}^\dagger c_{\gamma,\mathbf{k}\delta,\mathbf{k}'} c_{\lambda'\mathbf{k}''}} \\
&\bullet \quad c_{\lambda\mathbf{k}''}^\dagger c_{\lambda'\mathbf{k}''} c_{\alpha,\mathbf{k}+\mathbf{q}}^\dagger c_{\beta,\mathbf{k}'-\mathbf{q}}^\dagger c_{\gamma,\mathbf{k}\delta,\mathbf{k}'} = c_{\lambda\mathbf{k}''}^\dagger \delta_{\lambda',\alpha} \delta_{\mathbf{k}'',\mathbf{k}+\mathbf{q}} c_{\beta,\mathbf{k}'-\mathbf{q}}^\dagger c_{\gamma,\mathbf{k}\delta,\mathbf{k}'} - c_{\lambda\mathbf{k}''}^\dagger c_{\alpha,\mathbf{k}+\mathbf{q}}^\dagger c_{\lambda'\mathbf{k}''} c_{\beta,\mathbf{k}'-\mathbf{q}}^\dagger c_{\gamma,\mathbf{k}\delta,\mathbf{k}'} \\
&= c_{\lambda\mathbf{k}''}^\dagger \delta_{\lambda',\alpha} \delta_{\mathbf{k}'',\mathbf{k}+\mathbf{q}} c_{\beta,\mathbf{k}'-\mathbf{q}}^\dagger c_{\gamma,\mathbf{k}\delta,\mathbf{k}'} - c_{\lambda\mathbf{k}''}^\dagger c_{\alpha,\mathbf{k}+\mathbf{q}}^\dagger \delta_{\lambda'\beta} \delta_{\mathbf{k}'',\mathbf{k}'-\mathbf{q}} c_{\gamma,\mathbf{k}\delta,\mathbf{k}'} + \cancel{c_{\lambda\mathbf{k}''}^\dagger c_{\alpha,\mathbf{k}+\mathbf{q}}^\dagger c_{\beta,\mathbf{k}'-\mathbf{q}}^\dagger c_{\lambda'\mathbf{k}''} c_{\gamma,\mathbf{k}\delta,\mathbf{k}'}} \\
[H^{Coulomb}, c_{\lambda\mathbf{k}''}^\dagger c_{\lambda'\mathbf{k}''}] &= \sum_{\mathbf{k},\mathbf{k}',\mathbf{q}} \sum_{\alpha\beta\gamma\delta} W_{\mathbf{k},\mathbf{k}',\mathbf{q}}^{\alpha\beta\gamma\delta} (c_{\alpha,\mathbf{k}+\mathbf{q}}^\dagger c_{\beta,\mathbf{k}'-\mathbf{q}}^\dagger c_{\gamma,\mathbf{k}\delta,\mathbf{k}'} \delta_{\lambda,\delta} \delta_{\mathbf{k}',\mathbf{k}''} c_{\lambda'\mathbf{k}''} - c_{\alpha,\mathbf{k}+\mathbf{q}}^\dagger c_{\beta,\mathbf{k}'-\mathbf{q}}^\dagger \delta_{\lambda\gamma} \delta_{\mathbf{k}\mathbf{k}''} c_{\delta,\mathbf{k}'} c_{\lambda'\mathbf{k}''} \\
&\quad - c_{\lambda\mathbf{k}''}^\dagger \delta_{\lambda',\alpha} \delta_{\mathbf{k}'',\mathbf{k}+\mathbf{q}} c_{\beta,\mathbf{k}'-\mathbf{q}}^\dagger c_{\gamma,\mathbf{k}\delta,\mathbf{k}'} + c_{\lambda\mathbf{k}''}^\dagger c_{\alpha,\mathbf{k}+\mathbf{q}}^\dagger \delta_{\lambda'\beta} \delta_{\mathbf{k}'',\mathbf{k}'-\mathbf{q}} c_{\gamma,\mathbf{k}\delta,\mathbf{k}'} )
\end{aligned}$$

$$\begin{aligned}
&= \sum_{\mathbf{k}, \mathbf{k}', \mathbf{q}} \sum_{\alpha \beta \gamma \delta} W_{\mathbf{k}, \mathbf{k}', \mathbf{q}}^{\alpha \beta \gamma \delta} c_{\alpha, \mathbf{k}+\mathbf{q}}^\dagger c_{\beta, \mathbf{k}'-\mathbf{q}}^\dagger c_{\gamma, \mathbf{k}} \delta_{\lambda, \delta} \delta_{\mathbf{k}', \mathbf{k}''} c_{\lambda' \mathbf{k}''} - \sum_{\mathbf{k}, \mathbf{k}', \mathbf{q}} \sum_{\alpha \beta \gamma \delta} W_{\mathbf{k}, \mathbf{k}', \mathbf{q}}^{\alpha \beta \gamma \delta} c_{\alpha, \mathbf{k}+\mathbf{q}}^\dagger c_{\beta, \mathbf{k}'-\mathbf{q}}^\dagger \delta_{\lambda \gamma} \delta_{\mathbf{k} \mathbf{k}''} c_{\delta, \mathbf{k}'} c_{\lambda' \mathbf{k}''} \\
&- \sum_{\mathbf{k}, \mathbf{k}', \mathbf{q}} \sum_{\alpha \beta \gamma \delta} W_{\mathbf{k}, \mathbf{k}', \mathbf{q}}^{\alpha \beta \gamma \delta} c_{\lambda \mathbf{k}''}^\dagger \delta_{\lambda', \alpha} \delta_{\mathbf{k}'', \mathbf{k}+\mathbf{q}} c_{\beta, \mathbf{k}'-\mathbf{q}}^\dagger c_{\gamma, \mathbf{k}} c_{\delta, \mathbf{k}'} + \sum_{\mathbf{k}, \mathbf{k}', \mathbf{q}} \sum_{\alpha \beta \gamma \delta} W_{\mathbf{k}, \mathbf{k}', \mathbf{q}}^{\alpha \beta \gamma \delta} c_{\lambda \mathbf{k}''}^\dagger c_{\alpha, \mathbf{k}+\mathbf{q}}^\dagger \delta_{\lambda' \beta} \delta_{\mathbf{k}'', \mathbf{k}'-\mathbf{q}} c_{\gamma, \mathbf{k}} c_{\delta, \mathbf{k}'} \\
&= \sum_{\mathbf{k}, \mathbf{q}} \sum_{\alpha \beta \gamma} W_{\mathbf{k}, \mathbf{k}'', \mathbf{q}}^{\alpha \beta \gamma \lambda} c_{\alpha, \mathbf{k}+\mathbf{q}}^\dagger c_{\beta, \mathbf{k}''-\mathbf{q}}^\dagger c_{\gamma, \mathbf{k}} c_{\lambda' \mathbf{k}''} - \sum_{\mathbf{k}', \mathbf{q}} \sum_{\alpha \beta \delta} W_{\mathbf{k}'', \mathbf{k}', \mathbf{q}}^{\alpha \beta \lambda \delta} c_{\alpha, \mathbf{k}''+\mathbf{q}}^\dagger c_{\beta, \mathbf{k}'-\mathbf{q}}^\dagger c_{\delta, \mathbf{k}'} c_{\lambda' \mathbf{k}''} \\
&- \sum_{\mathbf{k}', \mathbf{q}} \sum_{\beta \gamma \delta} W_{\mathbf{k}'', \mathbf{k}', \mathbf{q}}^{\lambda' \beta \gamma \delta} c_{\lambda \mathbf{k}''}^\dagger c_{\beta, \mathbf{k}'-\mathbf{q}}^\dagger c_{\gamma, \mathbf{k}''-\mathbf{q}} c_{\delta, \mathbf{k}'} + \sum_{\mathbf{k}, \mathbf{q}} \sum_{\alpha \gamma \delta} W_{\mathbf{k}, \mathbf{k}', \mathbf{q}}^{\alpha \lambda' \gamma \delta} c_{\lambda \mathbf{k}''}^\dagger c_{\alpha, \mathbf{k}+\mathbf{q}}^\dagger c_{\gamma, \mathbf{k}} c_{\delta, \mathbf{k}''+\mathbf{q}} \\
&= \sum_{\mathbf{k}, \mathbf{q}} \sum_{\alpha \beta \gamma} W_{\mathbf{k}, \mathbf{k}'', \mathbf{q}}^{\alpha \beta \gamma \lambda} c_{\alpha, \mathbf{k}+\mathbf{q}}^\dagger c_{\beta, \mathbf{k}''-\mathbf{q}}^\dagger c_{\gamma, \mathbf{k}} c_{\lambda' \mathbf{k}''} - \sum_{\mathbf{k}', \mathbf{q}} \sum_{\alpha \beta \delta} W_{\mathbf{k}'', \mathbf{k}', \mathbf{q}}^{\alpha \beta \lambda \delta} c_{\alpha, \mathbf{k}''+\mathbf{q}}^\dagger c_{\beta, \mathbf{k}'-\mathbf{q}}^\dagger c_{\delta, \mathbf{k}'} c_{\lambda' \mathbf{k}''} \\
&- \sum_{\mathbf{k}', \mathbf{q}} \sum_{\beta \gamma \delta} W_{\mathbf{k}'', \mathbf{k}', \mathbf{q}}^{\lambda' \beta \gamma \delta} c_{\lambda \mathbf{k}''}^\dagger c_{\beta, \mathbf{k}'-\mathbf{q}}^\dagger c_{\gamma, \mathbf{k}''-\mathbf{q}} c_{\delta, \mathbf{k}'} + \sum_{\mathbf{k}, \mathbf{q}} \sum_{\alpha \gamma \delta} W_{\mathbf{k}, \mathbf{k}', \mathbf{q}}^{\alpha \lambda' \gamma \delta} c_{\lambda \mathbf{k}''}^\dagger c_{\alpha, \mathbf{k}+\mathbf{q}}^\dagger c_{\gamma, \mathbf{k}} c_{\delta, \mathbf{k}''+\mathbf{q}} \\
&= 2 \sum_{\mathbf{k}' \mathbf{q}} \left( \sum_{\alpha \beta \gamma} W_{\mathbf{k}'', \mathbf{k}', \mathbf{q}}^{\alpha \beta \gamma \lambda} c_{\alpha \mathbf{k}''+\mathbf{q}}^\dagger c_{\beta \mathbf{k}'-\mathbf{q}}^\dagger c_{\gamma \mathbf{k}'} c_{\lambda' \mathbf{k}''} + W_{\mathbf{k}', \mathbf{k}''+\mathbf{q}, \mathbf{q}}^{\alpha \lambda' \gamma \delta} c_{\lambda \mathbf{k}''}^\dagger c_{\alpha \mathbf{k}'+\mathbf{q}}^\dagger c_{\gamma \mathbf{k}''+\mathbf{q}} c_{\delta \mathbf{k}'} \right) \quad (65)
\end{aligned}$$

Using approximation for the 4-operators into the form of multiplication of 2-operators (Hartree-Fock approximation):

$$\begin{aligned}
\sum_{\mathbf{k}' \mathbf{q}} \left\langle c_{\alpha \mathbf{k}''+\mathbf{q}}^\dagger c_{\beta \mathbf{k}'-\mathbf{q}}^\dagger c_{\gamma \mathbf{k}'} c_{\lambda' \mathbf{k}''} \right\rangle &= - \sum_{\mathbf{k}' \mathbf{q}} \left\langle c_{\alpha \mathbf{k}''+\mathbf{q}}^\dagger c_{\gamma \mathbf{k}'} \right\rangle \left\langle c_{\beta \mathbf{k}'-\mathbf{q}}^\dagger c_{\lambda' \mathbf{k}''} \right\rangle \delta_{\mathbf{k}' \mathbf{k}''} \\
&= - \sum_{\mathbf{q}} \left\langle c_{\alpha \mathbf{k}''+\mathbf{q}}^\dagger c_{\gamma \mathbf{k}''+\mathbf{q}} \right\rangle \left\langle c_{\mathbf{k}''}^\dagger c_{\lambda' \mathbf{k}''} \right\rangle \quad (66)
\end{aligned}$$

$$\begin{aligned}
\sum_{\mathbf{k}' \mathbf{q}} \left\langle c_{\lambda \mathbf{k}''}^\dagger c_{\alpha \mathbf{k}'+\mathbf{q}}^\dagger c_{\gamma \mathbf{k}''+\mathbf{q}} c_{\delta \mathbf{k}'} \right\rangle &= \sum_{\mathbf{k}' \mathbf{q}} \left\langle c_{\lambda \mathbf{k}''}^\dagger c_{\delta \mathbf{k}'} \right\rangle \left\langle c_{\alpha \mathbf{k}'+\mathbf{q}}^\dagger c_{\gamma \mathbf{k}''+\mathbf{q}} \right\rangle \delta_{\mathbf{k}', \mathbf{k}''} \\
&= \sum_{\mathbf{q}} \left\langle c_{\lambda \mathbf{k}''}^\dagger c_{\delta \mathbf{k}''} \right\rangle \left\langle c_{\alpha \mathbf{k}''+\mathbf{q}}^\dagger c_{\gamma \mathbf{k}''+\mathbf{q}} \right\rangle \quad (67)
\end{aligned}$$

Include HFA (66) and (67) into (65). Take all the communication term (63), (64) and (65) into (41) to get the SBE in HFA:

$$\begin{aligned}
\frac{d}{dt} \rho_{\lambda \lambda'}(\mathbf{k}) &= -\frac{i}{\hbar} (\varepsilon_{\lambda}(\mathbf{k}) - \varepsilon_{\lambda'}(\mathbf{k})) \rho_{\lambda \lambda'} - \frac{ie}{\hbar m} \mathbf{A}(t) \sum_{\mu} (\mathbf{p}_{\lambda \mu}(\mathbf{k}) \rho_{\mu \lambda'}(\mathbf{k}) - \rho_{\lambda \mu}(\mathbf{k}) \mathbf{p}_{\mu \lambda'}(\mathbf{k})) \\
&+ \frac{i}{\hbar} (\Omega_{\lambda \mu}(\mathbf{k}) \rho_{\mu \lambda'}(\mathbf{k}) - \rho_{\lambda \mu}(\mathbf{k}) \Omega_{\mu \lambda'}(\mathbf{k})) \quad (68)
\end{aligned}$$



## C Dipole Matrix Elements

Starting from position matrix element:

$$\langle \psi_{\lambda \mathbf{k}} | \mathbf{r} | \psi_{\lambda' \mathbf{k}'} \rangle = \int \frac{d^3 r}{V} u_{\lambda \mathbf{k}}^*(\mathbf{r}) e^{-i \mathbf{k} \cdot \mathbf{r}} \mathbf{r} u_{\lambda' \mathbf{k}'}(\mathbf{r}) e^{i \mathbf{k}' \cdot \mathbf{r}} \quad (69)$$

$$\begin{aligned} &= i \nabla_{\mathbf{k}} \left( \int \frac{d^3 r}{V} e^{-i \mathbf{k} \cdot \mathbf{r}} u_{\lambda \mathbf{k}}^*(\mathbf{r}) u_{\lambda' \mathbf{k}'}(\mathbf{r}) e^{i \mathbf{k}' \cdot \mathbf{r}} \right) - \int \frac{d^3 r}{V} i e^{-i \mathbf{k} \cdot \mathbf{r}} (\nabla_{\mathbf{k}} u_{\lambda \mathbf{k}}^*) u_{\lambda' \mathbf{k}'} e^{i \mathbf{k}' \cdot \mathbf{r}} \\ &= i \nabla_{\mathbf{k}} \left( \frac{1}{N} \sum_i^N e^{i(\mathbf{k}' - \mathbf{k}) \cdot \mathbf{R}_i} \int_{V_{cell}} \frac{d^3 r}{V_{cell}} e^{-i \mathbf{k} \cdot \mathbf{r}} u_{\lambda \mathbf{k}}^*(\mathbf{r}) u_{\lambda' \mathbf{k}'}(\mathbf{r}) e^{i \mathbf{k}' \cdot \mathbf{r}} \right) \\ &\quad - i \frac{1}{N} \sum_i^N e^{i(\mathbf{k}' - \mathbf{k}) \cdot \mathbf{R}_i} \int_{V_{cell}} \frac{d^3 r}{V_{cell}} e^{i(\mathbf{k}' - \mathbf{k}) \cdot \mathbf{r}} (\nabla_{\mathbf{k}} u_{\lambda \mathbf{k}}^*) u_{\lambda' \mathbf{k}'} . \end{aligned} \quad (70)$$

Again, using the long-wavelength approximation to have

$$\langle \psi_{\lambda \mathbf{k}} | \mathbf{r} | \psi_{\lambda' \mathbf{k}'} \rangle \approx i \nabla_{\mathbf{k}} \delta_{\mathbf{k}, \mathbf{k}'} \delta_{\lambda \lambda'} - i \delta_{\mathbf{k}, \mathbf{k}'} \langle \nabla_{\mathbf{k}} u_{\lambda \mathbf{k}} | u_{\lambda' \mathbf{k}'} \rangle , \quad (71)$$

Define the dielectric matrix elements:

$$\xi_{\lambda \lambda'}(\mathbf{k}) = -i \langle \nabla_{\mathbf{k}} u_{\lambda \mathbf{k}} | u_{\lambda' \mathbf{k}'} \rangle , \quad (72)$$

Include this into (71) to have

$$\langle \psi_{\lambda \mathbf{k}} | \mathbf{r} | \psi_{\lambda' \mathbf{k}'} \rangle = \delta_{\mathbf{k}, \mathbf{k}'} (i \delta_{\lambda \lambda'} \nabla_{\mathbf{k}} + \xi_{\lambda \lambda'}(\mathbf{k})), \quad (73)$$

Using this relation along with (33) and  $[H_{1e}^0, \mathbf{r}] = -i \frac{\hbar}{m} \mathbf{p}$  for  $\lambda \neq \lambda'$ :

$$\xi_{\lambda \lambda'}(\mathbf{k}) = -\frac{i \hbar}{m} \frac{\mathbf{p}_{\lambda \lambda'}(\mathbf{k})}{\varepsilon_{\lambda}(\mathbf{k}) - \varepsilon_{\lambda'}(\mathbf{k})} \quad (74)$$

## References

- [1] Jie Jiang, Zhizhong Chen, Yang Hu, Yu Xiang, Lifu Zhang, Yiping Wang, Gwo-Ching Wang, and Jian Shi. Flexo-photovoltaic effect in MoS<sub>2</sub>. *Nat. Nanotechnol.*, 16(8):894–901, August 2021. Publisher: Nature Publishing Group.
- [2] William Shockley and Hans J. Queisser. Detailed Balance Limit of Efficiency of p-n Junction Solar Cells. *Journal of Applied Physics*, 32(3):510–519, March 1961.
- [3] B. I. Sturman. Ballistic and shift currents in the bulk photovoltaic effect theory. *Phys.-Usp.*, 63(4):407, April 2020. Publisher: IOP Publishing.
- [4] A. K. Geim and I. V. Grigorieva. Van der Waals heterostructures. *Nature*, 499(7459):419–425, July 2013. Publisher: Nature Publishing Group.
- [5] Qing Hua Wang, Kourosh Kalantar-Zadeh, Andras Kis, Jonathan N. Coleman, and Michael S. Strano. Electronics and optoelectronics of two-dimensional transition metal dichalcogenides. *Nature Nanotech.*, 7(11):699–712, November 2012.
- [6] Di Xiao, Wang Yao, and Qian Niu. Valley-Contrasting Physics in Graphene: Magnetic Moment and Topological Transport. *Phys. Rev. Lett.*, 99(23):236809, December 2007. Publisher: American Physical Society.
- [7] Wang Yao, Di Xiao, and Qian Niu. Valley-dependent optoelectronics from inversion symmetry breaking. *Phys. Rev. B*, 77(23):235406, June 2008. Publisher: American Physical Society.
- [8] Bumseop Kim, Noejung Park, and Jeongwoo Kim. Giant bulk photovoltaic effect driven by the wall-to-wall charge shift in WS<sub>2</sub> nanotubes. *Nat Commun*, 13(1):3237, June 2022. Publisher: Nature Publishing Group.
- [9] Y. J. Zhang, T. Ideue, M. Onga, F. Qin, R. Suzuki, A. Zak, R. Tenne, J. H. Smet, and Y. Iwasa. Enhanced intrinsic photovoltaic effect in tungsten disulfide nanotubes. *Nature*, 570(7761):349–353, June 2019. Publisher: Nature Publishing Group.
- [10] Dongyang Yang, Jingda Wu, Benjamin T. Zhou, Jing Liang, Toshiya Ideue, Teri Siu, Kashif Masud Awan, Kenji Watanabe, Takashi Taniguchi, Yoshihiro Iwasa, Marcel Franz, and Ziliang Ye. Spontaneous-polarization-induced photovoltaic effect in rhombohedrally stacked MoS<sub>2</sub>. *Nat. Photon.*, 16(6):469–474, June 2022. Publisher: Nature Publishing Group.
- [11] E. V. Kirichenko and V. A. Stephanovich. The influence of Coulomb interaction screening on the excitons in disordered two-dimensional insulators. *Sci Rep*, 11(1):11956, June 2021. Number: 1 Publisher: Nature Publishing Group.

- [12] Changjian Zhang, Haining Wang, Weimin Chan, Christina Manolatu, and Farhan Rana. Absorption of light by excitons and trions in monolayers of metal dichalcogenide  $\text{MoS}_2$ : Experiments and theory. *Phys. Rev. B*, 89(20):205436, May 2014. Publisher: American Physical Society.
- [13] Ashwin Ramasubramaniam. Large excitonic effects in monolayers of molybdenum and tungsten dichalcogenides. *Phys. Rev. B*, 86(11):115409, September 2012. Publisher: American Physical Society.
- [14] Diana Y. Qiu, Felipe H. da Jornada, and Steven G. Louie. Optical Spectrum of  $\text{MoS}_2$ : Many-Body Effects and Diversity of Exciton States. *Phys. Rev. Lett.*, 111(21):216805, November 2013. Publisher: American Physical Society.
- [15] Tawinan Cheiwchanchamnangij and Walter R. L. Lambrecht. Quasiparticle band structure calculation of monolayer, bilayer, and bulk  $\text{MoS}_2$ . *Phys. Rev. B*, 85(20):205302, May 2012. Publisher: American Physical Society.
- [16] Hongliang Shi, Hui Pan, Yong-Wei Zhang, and Boris I. Yakobson. Quasiparticle band structures and optical properties of strained monolayer  $\text{MoS}_2$  and  $\text{WS}_2$ . *Phys. Rev. B*, 87(15):155304, April 2013. Publisher: American Physical Society.
- [17] L. Meckbach, J. Hader, U. Huttner, J. Neuhaus, J. T. Steiner, T. Stroucken, J. V. Moloney, and S. W. Koch. Ultrafast band-gap renormalization and build-up of optical gain in monolayer  $\text{MoTe}_2$ . *Phys. Rev. B*, 101(7):075401, February 2020.
- [18] Timothy C. Berkelbach, Mark S. Hybertsen, and David R. Reichman. Theory of neutral and charged excitons in monolayer transition metal dichalcogenides. *Phys. Rev. B*, 88(4):045318, July 2013.
- [19] Gui-Bin Liu, Wen-Yu Shan, Yugui Yao, Wang Yao, and Di Xiao. Three-band tight-binding model for monolayers of group-VIB transition metal dichalcogenides. *Phys. Rev. B*, 88(8):085433, August 2013. Publisher: American Physical Society.
- [20] Di Xiao, Gui-Bin Liu, Wanxiang Feng, Xiaodong Xu, and Wang Yao. Coupled Spin and Valley Physics in Monolayers of  $\text{MoS}_2$  and Other Group-VI Dichalcogenides. *Phys. Rev. Lett.*, 108(19):196802, May 2012. Publisher: American Physical Society.
- [21] L. F. Mattheiss. Band Structures of Transition-Metal-Dichalcogenide Layer Compounds. *Phys. Rev. B*, 8(8):3719–3740, October 1973. Publisher: American Physical Society.
- [22] S. Lebegue and O. Eriksson. Electronic structure of two-dimensional crystals from ab initio theory. *Phys. Rev. B*, 79(11):115409, March 2009. Publisher: American Physical Society.

- [23] Z. Y. Zhu, Y. C. Cheng, and U. Schwingenschlögl. Giant spin-orbit-induced spin splitting in two-dimensional transition-metal dichalcogenide semiconductors. *Phys. Rev. B*, 84(15):153402, October 2011. Publisher: American Physical Society.
- [24] C. Ataca, H. Şahin, and S. Ciraci. Stable, Single-Layer MX<sub>2</sub> Transition-Metal Oxides and Dichalcogenides in a Honeycomb-Like Structure. *J. Phys. Chem. C*, 116(16):8983–8999, April 2012. Publisher: American Chemical Society.
- [25] Hartmut Haug and Stephan W. Koch. *Quantum Theory Of The Optical And Electronic Properties Of Semiconductors (5th Edition)*. World Scientific Publishing Company, January 2009. Google-Books-ID: 1J1IDQAAQBAJ.
- [26] Chendong Zhang, Amber Johnson, Chang-Lung Hsu, Lain-Jong Li, and Chih-Kang Shih. Direct Imaging of Band Profile in Single Layer MoS<sub>2</sub> on Graphite: Quasiparticle Energy Gap, Metallic Edge States, and Edge Band Bending. *Nano Lett.*, 14(5):2443–2447, May 2014. Publisher: American Chemical Society.
- [27] D. Erben, A. Steinhoff, C. Gies, G. Schönhoff, T. O. Wehling, and F. Jahnke. Excitation-induced transition to indirect band gaps in atomically thin transition-metal dichalcogenide semiconductors. *Phys. Rev. B*, 98(3):035434, July 2018.
- [28] D. Erben, A. Steinhoff, M. Lorke, and F. Jahnke. Optical nonlinearities in the excited carrier density of atomically thin transition metal dichalcogenides. *Phys. Rev. B*, 106(4):045409, July 2022.
- [29] Chau Duc Phuong Vo and Thanh Duc Huynh. Calculation of shift current tensors in two-dimensional transition metal dichalcogenides. *E3S Web Conf.*, 496:02002, 2024. Publisher: EDP Sciences.